Modeling and Three-Layer Adaptive Diving Control of a Cable-Driven Underwater Parallel Platform

YINGKAI XIA[1,2], KAN XU[3], YE LI[1], (Senior Member, IEEE), GUOHUA XU[2], AND XIANBO XIANG[2], (Member, IEEE)

[1]School of Naval Architecture, Ocean and Civil Engineering, Shanghai Jiao Tong University, Shanghai 200240, China
[2]School of Naval Architecture and Ocean Engineering, Huazhong University of Science and Technology, Wuhan 430074, China
[3]Wuhan Second Ship Design and Research Institute, Wuhan 430205, China

Corresponding authors: Ye Li (ye.li@sjtu.edu.cn) and Guohua Xu (hustxu@vip.sina.com)

ABSTRACT This paper focuses on the modeling, diving controller design, and experiment of a special cable-driven underwater parallel platform with eight-cable coupling drive structure. Kinematic and dynamic models of the platform are established utilizing a simplified approach, and the hydraulic driven control model is derived based on joint-space method. To improve the diving control precision and system robustness despite the complex dynamic behaviors and manifold unknown disturbances, a three-layer adaptive diving control strategy is proposed. Among the three control layers, layer 1 is responsible for dive planning and online monitoring, layer 2 places emphasis on synchronous control by employing an improved relative coupling strategy, layer 3 utilizes an adaptive radial basis function neural network-based backstepping sliding mode control algorithm (ARBFNN-BSMC) to achieve high precision speed control of the single driving branch. Hardware-in-the-loop simulations and experimental results illustrate that the proposed three-layer adaptive diving control strategy can asymptotically drive the cable-driven underwater parallel platform onto a predefined diving trajectory with favorable precision, robustness, and stability.

INDEX TERMS Cable-driven underwater parallel platform, modeling, three-layer adaptive diving control strategy, improved relative coupling synchronous control, ARBFNN-BSMC, experiment.

I. INTRODUCTION

Great attentions have been paid to ocean exploration considering the rich biological, energy, water, and metal resources. However, the oceanic environment is quite harsh and hostile such that humans are not capable of diving into deep sea or staying underwater for long time intervention [1]. Fortunately, this situation has been changed gradually with emergence of a wide variety of marine equipment.

Owing to excellent structural stability and carrying capability, marine platforms have become key structures for offshore exploration and production. Nevertheless, the research and application of marine platforms still face many difficulties considering the complex dynamic behavior and harsh oceanic environment.

Inspired by the recent developments in the field of marine platforms, a cable-driven underwater parallel platform is

proposed here. The current work focuses on the modeling and controller design of cable-driven underwater parallel platform with aim of accomplishing high precision diving control in practical experiment.

A. PLATFORM DESCRIPTION

As shown in Fig. 1, the cable-driven underwater parallel platform is required to dive to designated depth with experimental facilities of heavy load and provide a stable underwater testing basis. The main working process of cable-driven underwater parallel platform is implemented through three steps: Ballast adjusting, anchoring, and diving. The work reported here mainly discusses the problem of diving control.

To meet the load carrying capacity and stability requirements, the main body of platform is designed as a large rectangular cuboid with length of 50.4 m, width of 18 m,
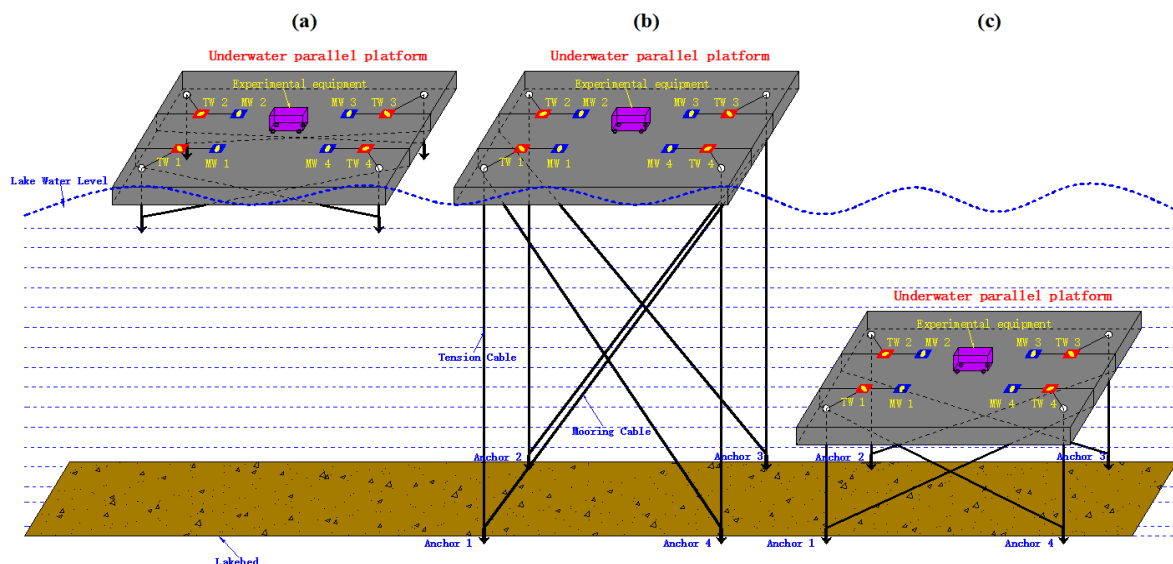
FIGURE 1. Application process description of cable-driven underwater parallel platform (TW denotes tension winch, MW denotes Mooring winch): (a) Ballast adjusting; (b) Anchoring; (c) Diving.

and height of 2 m. Four gravity anchors are carried by the platform itself, which are mainly used for underwater positioning. Eight hydraulic winches are installed on the surface of platform, acting as the main actuating devices, with eight cables connected to the four anchors. The distribution of the eight winches is uniform and symmetrical about the center of platform surface, and the four tension winches are closer to the four corners. Specific geometric parameters of the winch locations will be introduced in the appendix. The anchors, cables, and winches all together form an eight-cable coupling drive scheme, through which, vertical motion and attitude adjustment can be achieved.

Compared with conventional structures of underwater platforms, the proposed structure has following advantages:

1) Compared with independent anchoring scheme, the proposed structure has saved four anchors by connecting a pair of tension cable and mooring cable to the same gravity anchor.
2) The structure of platform is more stable owing to the eight-cable coupling drive scheme.
3) Considering the huge mass and size of platform, relatively gentle flow in the lake, as well as the effective constraints in horizontal direction provided by mooring cables, the movement and rotation of proposed platform in horizontal plane is limited to a large extent.

Although eight-cable coupling drive scheme improves the structural stability, it brings nonlinearity, cross-coupling, and a variety of uncertainties, making the dynamic behavior of platform more complex. Besides, due to requirements of test tasks, the attitudes of platform should stay in ideal state during the whole diving process. Considering the aforementioned object characteristics and control requirements, diving control is quite challenging. To complete the challenging task, modeling, controller design, and experimental validation are discussed in this work.

B. RELATED WORKS
1) MODELING
The structure of cable-driven underwater parallel platform is similar to the classical Gough-Stewart platform [2]. Owing to the favorable dexterity, stability, response speed, and load carrying capacity, platforms of Gough-Stewart structure have been widely used. Nevertheless, precise modeling for such a parallel platform is a difficult task, which always results in a set of highly coupled nonlinear equations. An increasing number of papers have addressed the topic of modeling for parallel platforms, and the frequently used methods include: Lagrangian [3], Newton–Euler [4], Kane [5], and Principle of virtual work [6].

Long et al. [7] presented a method for calculating the direct and inverse dynamic models of a parallel robot with a flexible platform, where the platform is treated as a flexible body whereas the links of the legs are considered as rigid. Wu et al. [8] derived the mechatronics model of a 2-DOF parallel manipulator in a 5-DOF hybrid machine tool using bond graph. Nguyen et al. [9] utilized a matrix structure analysis method to derive the static and dynamic models of a parallel robot manipulator. Horoub et al. [10] analyzed the dynamic behavior of Gough-Stewart type cable marine platform in the framework of rigid-body dynamics, and estimated the water wave loading by integral methods. Cai et al. [11] proposed a 6-degree of freedom (DOF) serial-parallel precision positioning system by combining two compact type 3-DOF parallel mechanisms, and derived the kinematic and dynamic models.

2) CONTROL
Owing to the unique structure and unknown disturbances, the cable-driven underwater parallel platform has complex time-varying models with unknown uncertainties. Designing a controller to regulate such a complex system is not easy. For

complex nonlinear systems with uncertainties, the commonly used control methods include but not limited to H_∞ control [12], adaptive control [13], sliding-mode control [14], fuzzy-logic control [15], backstepping control [16], and neural network methods [17]. In recent works, disturbance estimation and system robustness improvement have become two major research priorities.

The parameter uncertainties and unknown external disturbances in controller design should be taken into account since they could severely degrade the system performance. In recent years, neural network [18] and disturbance observer [19] are two of the main solutions for system uncertainty estimation. Mirza et al. [20] established a model-free dual neural network to learn the unknown time-varying parameters of a Stewart platform. Fang et al. [21] proposed an adaptive decoupling control method for three-axis gyro stabilized platform, which estimated the uncertainties by the RBF neural networks, and the parameters of the NNs can be modified in real-time with the proposed adaptive decoupling control algorithm. Zhang et al. [22] proposed an observer-based optimal fault-tolerant control method for an offshore steel jacket platform, which achieved real-time observation and improved the reliability of the offshore platform a lot.

Meanwhile, since the model estimation accuracy cannot be absolutely guaranteed, the robustness of control scheme is of major importance [23]. Sliding mode control is an effective method for nonlinear system since it can enhance robustness of a control system regardless of the external disturbances and parameter variations. Nourisola et al. [24] introduced several new types of adaptive sliding mode controllers to solve the control problem for an offshore steel jacket platform subject to nonlinear wave-induced force. In [25], a decoupled double closed-loop control strategy is proposed for an underwater tension leg platform, and internal closed-loop controllers are designed and tested based on backstepping sliding mode control method. Zhang et al. [26] designed a robust integral sliding mode controller for an offshore steel jacket platform subject to nonlinear wave-induced force and parameter perturbations, which reduced the internal oscillations dramatically.

C. OBJECTIVE OF THIS WORK

To achieve high-precision diving control of cable-driven underwater parallel platform regardless of complex dynamic behavior and manifold unknown disturbances, the current work focuses on modeling, diving controller design, and experiment. The main contributions of this work are summarized as follows.

1) A simplified modeling method is proposed for such a complex system, which obtains the kinematic and dynamic models of platform within a three degrees-of-freedom framework, and derives the joint-space driven control model.

2) To overcome model uncertainties and achieve adaptive robust diving control, a three-layer adaptive diving control strategy is proposed, where improved relative coupling strategy is adopted to achieve synchronous control, and adaptive radial basis function neural network based backstepping sliding mode control (ARBFNN-BSMC) is utilized to improve the speed control precision, robustness, and anti-jamming ability.

3) Hardware-in-the-loop simulations and early-stage experiments are carried out to validate the feasibility and efficiency of the proposed three-layer adaptive diving control.

The rest of this work is organized as follows. Section II establishes the models, and describes the diving control problem. Section III proposes a three-layer adaptive diving control strategy and presents the controller design process. Section IV validates the previous analysis and design through hardware-in-the-loop simulations. Section V demonstrates the experiment results. Section VI concludes this work and describes the future research avenues.

II. MODELING AND PROBLEM FORMULATION
A. KINEMATICS

As shown in Fig. 2, two reference frames are established: earth-fixed frame, $\{O\} := (O - X, Y, Z)$, and body-fixed frame, $\{O_1\} := (O_1 - X_1, Y_1, Z_1)$ [27]. Frame $\{O\}$ is established on the water surface, whereas $\{O_1\}$ is established on the parallel platform. Origin O_1 is fixed at the geometric center on the surface of the platform, and axis $O_1 X_1$ is pointing to the bow.
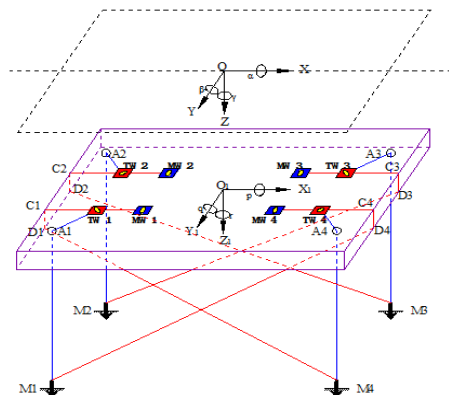

FIGURE 2. Reference frames and motion parameters description.

The vector relationship of single drive branch i is depicted in Fig. 3.

Let L_i be the length of drive branch i, and e_i denote the unit direction vector, the position vector of drive branch i in frame $\{O\}$ is given by

$$\overrightarrow{L_i} = L_i \cdot e_i = \overrightarrow{OO_1} + R_{O_1}^O \overrightarrow{O_1 M_i} - \overrightarrow{OA_i} \tag{1}$$

where, $R_{O_1}^O$ denotes the rotation matrix.

Let (x_i, y_i, z_i) be the position vector of A_i in the frame $\{O\}$. Let h_i be the vertical deviation between M_i and O_1. Define $a' = |A_1 A_4|$, $b' = |A_1 A_2|$, the position vectors of four drive
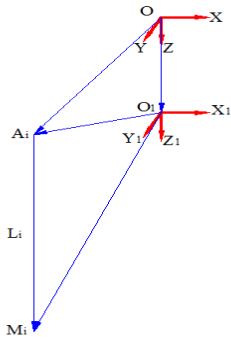
FIGURE 3. Vector relationship of single drive branch *i*.

branches can be expressed as

$$
\overrightarrow{L_1} = \begin{bmatrix} x - x_1 - \frac{a'}{2}\cos\alpha + \frac{b'}{2}\sin\beta\sin\alpha + h_1\cos\beta\sin\alpha \\ y - y_1 + \frac{b'}{2}\cos\beta - h_1\sin\beta \\ z - z_1 + \frac{a'}{2}\sin\alpha + \frac{b'}{2}\sin\beta\cos\alpha + h_1\cos\beta\cos\alpha \end{bmatrix}
\tag{2}
$$

$$
\overrightarrow{L_2} = \begin{bmatrix} x - x_2 - \frac{a'}{2}\cos\alpha - \frac{b'}{2}\sin\beta\sin\alpha + h_2\cos\beta\sin\alpha \\ y - y_2 - \frac{b'}{2}\cos\beta - h_2\sin\beta \\ z - z_2 + \frac{a'}{2}\sin\alpha - \frac{b'}{2}\sin\beta\cos\alpha + h_2\cos\beta\cos\alpha \end{bmatrix}
\tag{3}
$$

$$
\overrightarrow{L_3} = \begin{bmatrix} x - x_3 + \frac{a'}{2}\cos\alpha - \frac{b'}{2}\sin\beta\sin\alpha + h_3\cos\beta\sin\alpha \\ y - y_3 - \frac{b'}{2}\cos\beta - h_3\sin\beta \\ z - z_3 - \frac{a'}{2}\sin\alpha - \frac{b'}{2}\sin\beta\cos\alpha + h_3\cos\beta\cos\alpha \end{bmatrix}
\tag{4}
$$

$$
\overrightarrow{L_4} = \begin{bmatrix} x - x_4 + \frac{a'}{2}\cos\alpha + \frac{b'}{2}\sin\beta\sin\alpha + h_4\cos\beta\sin\alpha \\ y - y_4 + \frac{b'}{2}\cos\beta - h_4\sin\beta \\ z - z_4 - \frac{a'}{2}\sin\alpha + \frac{b'}{2}\sin\beta\cos\alpha + h_4\cos\beta\cos\alpha \end{bmatrix}
\tag{5}
$$

Specially, if $\alpha = \beta = 0$, the position coordinate matrix of drive branch *i* can be simplified as

$$
\overrightarrow{L_i} = \begin{bmatrix} 0 \\ 0 \\ h_i \end{bmatrix}
\tag{6}
$$

The position vectors of tension cables can be solved by (1)-(5). After that, the position vectors of mooring cables can be derived according to the geometric relationship between tension cables and mooring cables, as shown in Fig. 4.

Actually, $A_1 M_1$ and $D_4 M_1$ represent the effective lengths of tension cable 1 and mooring cable 4 respectively. Define $A_1 E_4 = a_\triangle$, $C_4 E_4 = b_\triangle$, one can obtain

$$
L'^2_4 = (L_1 - C_4 D_4)^2 + a_\triangle^2 + b_\triangle^2
\tag{7}
$$

Then, length of mooring cable 4 is calculated by

$$
L'_4 = \sqrt{(L_1 - C_4 D_4)^2 + a_\triangle^2 + b_\triangle^2}
\tag{8}
$$

Other lengths of mooring cables can be obtained by the similar approach. Therefore, the lengths of tension cables and mooring cables can be calculated. Let $\overrightarrow{L_{i1}}$ denote the
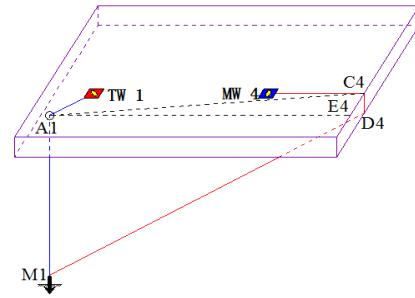
previous position vector of cable *i*, and $\overrightarrow{L_{i2}}$ denote the current position vector of cable *i*, the length variation of cable *i* can be calculated by

$$
\Delta L_i = \left| \overrightarrow{L_{i2}} \right| - \left| \overrightarrow{L_{i1}} \right|
\tag{9}
$$

Hence, the angle variation of corresponding hydraulic winch *i* can be obtained by

$$
\theta_{mi} = \frac{n \Delta L_i}{R}
\tag{10}
$$

where, θ_{mi} denotes the angle variation of hydraulic winch *i*, *n* denotes the reduction ratio, *R* denotes the radius.

B. PLATFORM DYNAMICS

To facilitate dynamic modeling of underwater platform, following assumptions are required.

Assumption 1: The platform is a rigid body;

Assumption 2: The mass distribution of the platform is uniform, and it's geometric symmetry.

Apart from the abovementioned assumptions, following three remarks should also be declared.

Remark 1: Owing to the eight-cable coupling driving scheme, great mass, great dimensions, and relatively gentle flow in the lake, the movement and rotation of proposed platform in horizontal plane is limited to a large extent. Moreover, according to CFD calculation, the horizontal moving displacements caused by lake current can almost be ignored when compared with dimensions of the platform.

Remark 2: Properties of the cables may affect the control of platform. For instance, the occasional jittering effect may influence the diving stability. However, such characteristics are difficult to measure and quantify. To compensate for that, they are treated as uncertainties, and a corrected dynamic model is established based on the standard dynamic modeling and uncertainties analyses.

Remark 3: Based on the abovementioned assumptions and remarks, it can be concluded that roll, pitch, and heave are the dominant components of motion. Therefore, to simplify the modeling process, the dynamics equation of underwater parallel platform is established within a three degrees-of-freedom framework, and the emphasis of force analysis is put on the forces of vertical direction.

FIGURE 4. The geometric relationship between tension cable 1 and mooring cable 4.

Force analysis of the proposed platform in vertical plane is shown in Fig. 5.
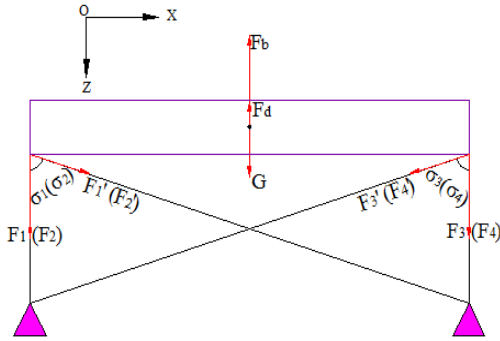

FIGURE 5. Force analysis of platform in vertical plane.

According to Newton-Euler method, dynamics equation of underwater parallel platform can be expressed as (11), shown at the bottom of this page,

where, m_1 denotes the mass of platform, Δm denotes the additional mass, I_x is the lateral inertia tensor, I_y is the longitudinal inertia tensor, ΔI_x is the additional lateral inertia tensor, ΔI_y is the additional longitudinal inertia tensor, G denotes the gravity force, F_b represents the buoyancy, F_d denotes the viscous water resistance caused by vertical moving, $F_i(i = 1, 2, 3, 4)$ represent the forces of four tension cables, $F_i'(i = 1, 2, 3, 4)$ represent the forces of four mooring cables, $\sigma_i(i = 1, 2, 3, 4)$ represent the angles between mooring cables and vertical direction, $a'/2$ and $b'/2$ are the effective actuating arm lengths of tension cables, $a''/2$ and $b''/2$ are the effective actuating arm lengths of mooring cables.

Viscous water resistance is derived by $F_d = 0.5C_d\rho_0 v^2 A$, which is positively related to the vertical velocity of platform. When the platform is diving with a nominal velocity $v =$

1.5m/ min, the viscous water resistance is 343.1 N, which can be ignored compared with the cable forces, platform gravity, and buoyancy. To simplify the dynamic models, F_d is out of consideration in the following deriving process, whereas is treated as disturbance in corrected joint-space driven control model.

Based on the above analysis, (11) can be transformed in vector form as

$$\mathbf{L_f} \cdot \mathbf{F} + \mathbf{M_g} = \mathbf{M_L}\ddot{\eta} \qquad (12)$$

where, $\mathbf{L_f}$ is the actuating arm matrix, $\mathbf{F}$ is the drive matrix, $\mathbf{M_g}$ is the equivalent gravity matrix, $\mathbf{M_L}$ is the inertia matrix, η is the dominant motion parameter matrix.

C. HYDRAULIC DYNAMICS

The core theory of hydraulic winches can be simplified as a valve-controlled hydraulic motor system, and its scheme is shown in Fig. 6. To facilitate the hydraulic dynamic modeling, following assumptions are required.
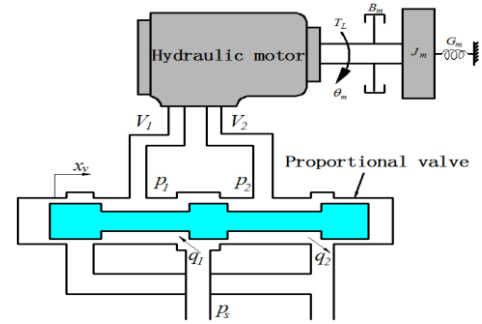

FIGURE 6. Schematic model of the hydraulic drive system.

Assumption 3: All pipes are short and thick, such that the pipe friction loss, fluid mass impaction, and pipe dynamic can be ignored;

$$
\begin{bmatrix}
1 & 1 & 1 & 1 & \cos\sigma_1 & \cos\sigma_2 & \cos\sigma_3 & \cos\sigma_4 \\
\dfrac{b'}{2} & -\dfrac{b'}{2} & -\dfrac{b'}{2} & \dfrac{b'}{2} & \dfrac{b''}{2}\cos\sigma_1 & -\dfrac{b''}{2}\cos\sigma_2 & -\dfrac{b''}{2}\cos\sigma_3 & \dfrac{b''}{2}\cos\sigma_4 \\
-\dfrac{a'}{2} & -\dfrac{a'}{2} & \dfrac{a'}{2} & \dfrac{a'}{2} & -\dfrac{a''}{2}\cos\sigma_1 & -\dfrac{a''}{2}\cos\sigma_2 & \dfrac{a''}{2}\cos\sigma_3 & \dfrac{a''}{2}\cos\sigma_4
\end{bmatrix}
\begin{bmatrix} F_1 \\ F_2 \\ F_3 \\ F_4 \\ F_1' \\ F_2' \\ F_3' \\ F_4' \end{bmatrix}
+
\begin{bmatrix} G - F_d - F_b \\ 0 \\ 0 \end{bmatrix}
$$

$$
=
\begin{bmatrix}
m_1 + \Delta m & 0 & 0 \\
0 & I_x + \Delta I_x & 0 \\
0 & 0 & I_y + \Delta I_y
\end{bmatrix}
\begin{bmatrix} \ddot{z} \\ \ddot{\alpha} \\ \ddot{\beta} \end{bmatrix}
\qquad (11)
$$

Assumption 4: Pressure in each chamber of the motor is equal everywhere, oil temperature and bulk modulus are constant;

Assumption 5: Internal and external leakage flow of the hydraulic motor is laminar flow.

The hydraulic dynamics can be described using the following four equations [28].

1) **Spool control equation**

$$X_v = Ku \tag{13}$$

where, X_v denotes the opening of valve spool, K denotes the gain of proportional valve, u denotes the input voltage.

2) **Flow equation**

$$Q_L = C_d \omega Ku \sqrt{\frac{1}{\rho}(P_s - P_L)} \tag{14}$$

where, Q_L denotes the load flow, C_d denotes the flow coefficient of valve port, ω denotes the area gradient, P_S denotes the oil-supply pressure of the pump, P_L denotes the load pressure, ρ denotes the hydraulic oil density.

3) **Continuity equation**

$$Q_L = D_m s \theta_m + \left(C_{tm} + \frac{V_m}{4\beta_e}s\right) p_L \tag{15}$$

where, D_m is the theoretical volumetric displacement of the hydraulic motor, θ_m is the rotate angle of motor rotor, C_{tm} is the total leakage coefficient, V_m is the total volume of actuation mechanism, and β_e denotes the effective bulk modulus of the system.

4) **Torque balance equation**

$$T_s = D_m p_L = \left(J_m s^2 + B_m s + G_m\right)\theta_m + T_L \tag{16}$$

where, T_s is the total torque generated by hydraulic motor and external load, J_m is the inertia of hydraulic motor and load, B_m represents the viscous damping coefficient of hydraulic motor and load, G_m is the torsional stiffness of the load springs, and T_L denotes the external load torque.

D. JOINT-SPACE DRIVEN DYNAMICS

Joint-space method is utilized to derive the hydraulic driven control model.

Following equation can be obtained based on (12).

$$\ddot{\eta} = \mathbf{M_L^{-1} L_f} \cdot \mathbf{F} + \mathbf{M_L^{-1} M_g} \tag{17}$$

The joint-space input acceleration is obtained based on linear transmission function $\dot{l} = J_\eta \dot{\eta}$ as

$$\ddot{\mathbf{L}} = J_\eta \mathbf{M_L^{-1} L_f} \cdot \mathbf{F} + J_\eta \mathbf{M_L^{-1} M_g} \tag{18}$$

where, L denotes the joint-space displacement matrix, and J_η is the Jacobian matrix.

Based on mechanical transmission principle, one can obtain

$$\frac{R}{n}\ddot{\boldsymbol{\theta}}_{\mathbf{m}} = J_\eta \mathbf{M_L^{-1} L_f} \cdot \mathbf{F} + J_\eta \mathbf{M_L^{-1} M_g} \tag{19}$$

Therefore, the force equation of tension winch is expressed as

$$\mathbf{F} = (J_\eta \mathbf{M_L^{-1} L_f})^{-1}(\frac{R}{n}\ddot{\boldsymbol{\theta}}_{\mathbf{m}} - J_\eta \mathbf{M_L^{-1} M_g}) \tag{20}$$

Then, the external load torque vector of hydraulic winch is calculated using $T = R \cdot F / n$ as

$$\mathbf{T_L} = \frac{R}{n}(J_\eta \mathbf{M_L^{-1} L_f})^{-1}(\frac{R}{n}\ddot{\boldsymbol{\theta}}_{\mathbf{m}} - J_\eta \mathbf{M_L^{-1} M_g}) \tag{21}$$

Substituting (21) into (16), one can obtain the new torque balance equation of hydraulic drive system as

$$\begin{aligned}
T_s = p_L D_m &= J_m \frac{d^2\theta_m}{dt^2} + B_m \frac{d\theta_m}{dt} + G_m \theta_m \\
&+ \frac{R}{n}(J_\eta M_L^{-1} L_f)^{-1}(\frac{R}{n}\ddot{\theta}_m - J_\eta M_L^{-1} M_g)
\end{aligned} \tag{22}$$

Hence, the joint-space driven control model is obtained by (13)-(16) and (22) as

$$\begin{cases}
x_v = Ku \\
Q_L = c_d \omega x_v \sqrt{\frac{1}{\rho}(p_s - p_L \mathrm{sgn}(x_v))} \\
Q_L = D_m \frac{d\theta_m}{dt} + C_{tm} p_L + \frac{V_m}{4\beta_e}\frac{dp_L}{dt} \\
T_s = p_L D_m = J_m \frac{d^2\theta_m}{dt^2} + B_m \frac{d\theta_m}{dt} + G_m \theta_m \\
\qquad + \frac{R}{n}(J_\eta M_L^{-1} L_f)^{-1}(\frac{R}{n}\ddot{\theta}_m - J_\eta M_L^{-1} M_g)
\end{cases} \tag{23}$$

After a series of transformations, the joint-space driven control model described in (23) is rewritten as

$$\begin{cases}
(J_m + (J_\eta M_L^{-1} L_f)^{-1}\frac{R^2}{n^2})\ddot{\theta}_m \\
= -B_m \dot{\theta}_m - G_m \theta_m + \frac{R}{n}(J_\eta M_L^{-1} L_f)^{-1} J_\eta M_L^{-1} M_g + T_s \\
\frac{V_m}{4\beta_e D_m}\dot{T}_s \\
= -D_m \dot{\theta}_m - \frac{C_{tm} T_s}{D_m} + c_d \omega Ku \sqrt{\frac{1}{\rho}(p_s - p_L \mathrm{sgn}(u))}
\end{cases} \tag{24}$$

Assume the elastic force is ignored ($G_m = 0$), (24) can be further expressed as

$$\begin{cases}
\ddot{\theta}_m = a_1 \dot{\theta}_m + a_2 T_s + a_3 \\
\dot{T}_s = b_1 \dot{\theta}_m + b_2 T_s + b_3 u
\end{cases} \tag{25}$$

Where,

$$a_1 = \frac{-B_m}{J_m + (J_\eta M_L^{-1} L_f)^{-1}\frac{R^2}{n^2}};$$

$$a_2 = \frac{1}{J_m + (J_\eta M_L^{-1} L_f)^{-1}\frac{R^2}{n^2}};$$

$$a_3 = \frac{1}{J_m + (J_\eta M_L^{-1} L_f)^{-1} \frac{R^2}{n^2}} \frac{R}{n} (J_\eta M_L^{-1} L_f)^{-1} J_\eta M_L^{-1} M_g;$$

$$b_1 = \frac{-4\beta_e D_m^2}{V_m};$$

$$b_2 = \frac{-4\beta_e C_{tm}}{V_m};$$

$$b_3 = \frac{-4\beta_e D_m}{V_m} c_d \omega K \sqrt{\frac{1}{\rho}(p_s - p_L \mathrm{sgn}(u))}.$$

Considering the complex object properties and unknown working environment, parameter uncertainties and un-modeled uncertainties may exist. Let Δa_1, Δa_2, Δa_3, Δb_1, Δb_2, and Δb_3 be the parameter uncertainties, Δ_1 and Δ_2 be the un-modeled uncertainties, (25) is further described as

$$\begin{cases} \ddot{\theta}_m = (a_1 + \Delta a_1)\dot{\theta}_m + (a_2 + \Delta a_2)T_s + a_3 + \Delta a_3 + \Delta_1 \\ \dot{T}_s = (b_1 + \Delta b_1)\dot{\theta}_m + (b_2 + \Delta b_2)T_s + (b_3 + \Delta b_3)u + \Delta_2 \end{cases}$$
(26)

If we define $\lambda_1 = \Delta a_1 \dot{\theta}_m + \Delta a_2 T_s + \Delta a_3 + \Delta_1$ and $\lambda_2 = \Delta b_1 \dot{\theta}_m + \Delta b_2 T_s + \Delta b_3 u + \Delta_2$, then corrected joint-space driven control model is presented by

$$\begin{cases} \ddot{\theta}_m = a_1 \dot{\theta}_m + a_2 T_s + a_3 + \lambda_1 \\ \dot{T}_s = b_1 \dot{\theta}_m + b_2 T_s + b_3 u + \lambda_2 \end{cases}$$
(27)

where, λ_1 and λ_2 are compound uncertainties, which contain parameter uncertainties and un-modeled uncertainties.

To facilitate controller design in the next section, following assumption is required.

Assumption 6: The uncertainties of corrected joint-space driven control model satisfy $|\lambda_i| \leq \varphi_i$, where $\varphi_i (i = 1, 2)$ are unknown positive constants.

E. PROBLEM FORMULATION

According to the special requirements of scientific research, as well as the endurance of the experimental equipment, following diving control requirements should be met for the underwater parallel platform.

1) Depth requirement: The ultimate diving depth ranges from 40 m to 100 m, and the ultimate depth control error should be less than 0.5 m;
2) Speed requirement: The ideal diving speed ranges from 1.5 m/min to 2.5 m/min, and the steady-state speed control error should be less than 5%;
3) Attitude requirement: $|\alpha| \leq 3°$, $|\beta| \leq 2°$.

Our objective is to design a control law for proposed platform to asymptotically reach to the desired depth according to the diving requirements, regardless of complex dynamic behaviors and various disturbances. Considering the object characteristics and diving control requirements, the design process should include following three parts: 1) General dive planning and monitoring based on kinematic model. 2) Synchronous control based on cross-coupling relationship between hydraulic winches. 3) Adaptive robust speed control of hydraulic winches based on corrected joint-space driven control model.

The previous problems are mathematically stated as follows:

Problem 1: Given a desired depth z_d, desired attitudes α and β, derive a control law to generate the input speed instructions of eight hydraulic winches $\dot{\theta}_{mi}(i = 1, 2, 3, 4)$ and $\dot{\theta}'_{mi}(i = 1, 2, 3, 4)$, according to the inverse kinematics solution and actual state feedback of the platform, so that the depth error $z - z_d$ can tend uniformly and asymptotically to zero with required attitudes: $|\alpha| \leq 3°$, $|\beta| \leq 2°$.

Problem 2: Given the ideal speed instructions of four tension winches $\dot{\theta}_{mi}(i = 1, 2, 3, 4)$, and four mooring winches $\dot{\theta}'_{mi}(i = 1, 2, 3, 4)$, derive a synchronous control law to generate the speed adjusting instructions $\Delta\dot{\theta}_{mi}(i = 1, 2, 3, 4)$ and $\Delta\dot{\theta}'_{mi}(i = 1, 2, 3, 4)$, according to the actual speed deviation between each winch, so that the synchronization between each winch is enhanced and the diving process will be more stable.

Problem 3: Given the corrected input speed instruction $\dot{\theta}_m + \Delta\dot{\theta}_m$, derive an adaptive robust control law u according to the corrected joint-space driven control model and actual speed error, so that the speed control accuracy, robustness, and stability can be ensured regardless of compound uncertainties.

III. DIVING CONTROLLER DESIGN
A. THREE-LAYER ADAPTIVE DIVING CONTROL STRATEGY

To improve the diving control precision and system robustness despite the complex dynamic behaviors and manifold unknown disturbances, a three-layer adaptive diving control strategy is proposed here, with schematic diagram shown in Fig. 7. The adaptive diving control strategy mainly contains following three layers.

Layer 1 (Dive Planning and General Monitoring): Layer 1 is responsible for dive planning and general monitoring. On the one hand, the diving mission is analyzed, and ideal speed control instructions of hydraulic winches are derived based on inverse kinematic solution. On the other hand, depth and attitude of underwater parallel platform are being monitored all the time, and once transfinite attitude appears, speed control instructions of hydraulic winches will be adjusted.

Layer 2 (Synchronous Control):

Two synchronous controllers are established, one for tension winches, and the other one for mooring winches. According to the speed control instructions and actual states of hydraulic winches, synchronous speed adjustments are derived by synchronous controllers. Considering the potential working conditions, an improved relative coupling strategy is utilized for synchronous control.

Layer 3 (Speed Control):

Speed control is the innermost layer for diving process, the precision and robustness of which will affect the synchronization and stability of diving process directly. To overcome the effects of unknown system uncertainties and achieve adaptive robust control, an ARBFNN-BSMC algorithm is utilized.
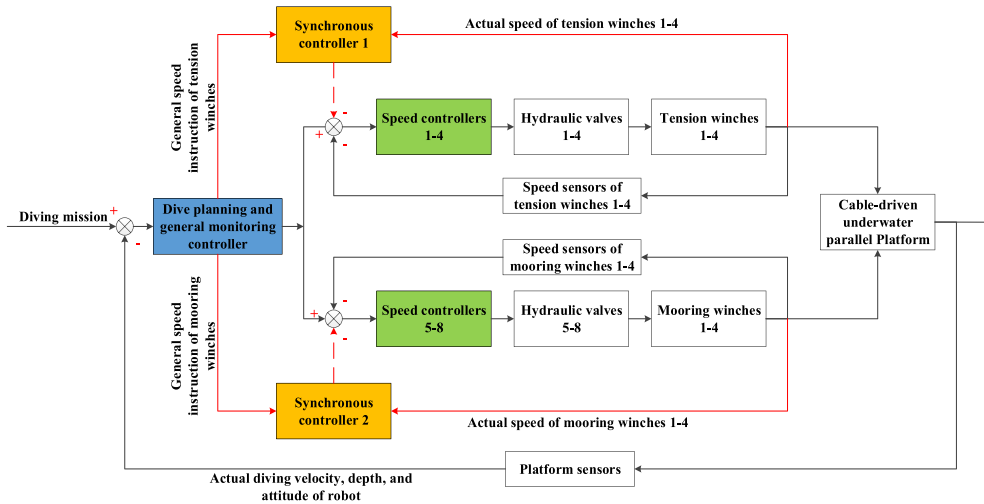
FIGURE 7. Scheme of three-layer adaptive diving control strategy.

B. CONTROLLER DESIGN OF LAYER 1

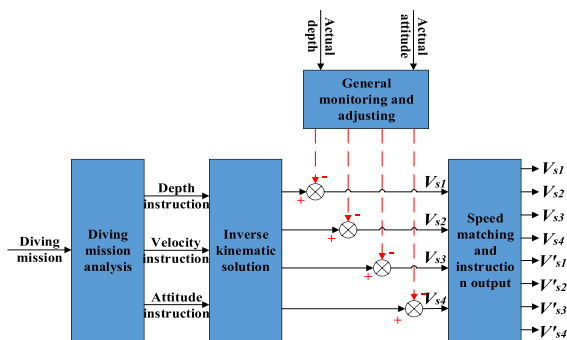The scheme of dive planning and general monitoring controller is shown in Fig. 8.

FIGURE 8. Scheme of dive planning and general monitoring controller.

The dive planning and general monitoring can be achieved by the following three steps.

Step 1 (Ideal Speed Instruction Acquisition):

Ideal speed instructions of four tension winches are obtained according to the diving mission and inverse kinematic solution, as derived in section II.A.

Step 2 (Monitoring and Speed Instruction Adjusting):

During the diving process, the depth and attitude are being monitored all the time, if the attitude of platform is beyond safety range (To implement advanced intervention, the safety attitude range is set as $|\alpha| < 1.5°$, $|\beta| < 1°$), active speed instruction adjustment will be carried out.

The speed instruction adjusting method is given by

$$V_{si} = V_{ti} - f(\Delta d_{li}), \quad (i = 1, 2, 3, 4) \qquad (28)$$

where, V_{ti} denotes the ideal speed instruction, $f(\Delta d_{li})$ denotes the speed adjusting function. The parameter Δd_{li} denotes the depth derivation of drive branch i, $\Delta d_{li} = d_{li} - d_0$, where d_{li}

denotes the depth of drive branch i, d_0 denotes the depth of platform, which are measured by the depth sensors.

In order to adjust the platform attitudes back to normal, following constraint conditions are required.

$$\begin{cases} f(\Delta d_{li}) > 0, & \Delta d_{li} > 0; \\ f(\Delta d_{li}) = 0, & \Delta d_{li} = 0; \quad (i = 1, 2, 3, 4) \\ f(\Delta d_{li}) < 0, & \Delta d_{li} < 0; \end{cases} \qquad (29)$$

Hence, following proportional adjusting method is utilized to calculate the speed adjustment value

$$f(\Delta d_{li}) = \frac{V_{ti}}{\varepsilon_i} \cdot \Delta d_{li}, \quad (i = 1, 2, 3, 4) \qquad (30)$$

where, ε_i denotes the proportional factor.

Therefore, the speed instructions of tension winches after adjustment are described as

$$V_{si} = V_{ti} - f(\Delta d_{li}) = V_{ti} - \frac{V_{ti}}{\varepsilon_i} \cdot \Delta d_{li}, \quad (i = 1, 2, 3, 4) \qquad (31)$$

Step 3 (Speed Matching and Instruction Output):

The speeds of the mooring winches are positively related to the speeds of corresponding tension winches. To simplify the control process, mooring winches are controlled in following-up mode, which means the speed control instructions for mooring winches are generated based on the coupling relationship between mooring cable and corresponding tension cable, as described in (8).

C. CONTROLLER DESIGN OF LAYER 2

The synchronization between each drive branch influences not only the control precision, but also the diving stability. To enhance the synchronization, an improved relative coupling control scheme is utilized, which employs scale quantization and compensation. The improved relative
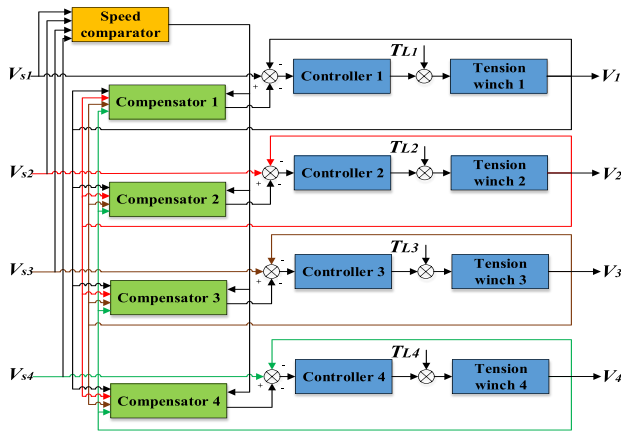
FIGURE 9. Improved relative coupling synchronous control strategy.

coupling synchronous control scheme used for four tension winches is shown in Fig. 9.

The schemes of speed comparator and compensator 1 are presented in Fig. 10.
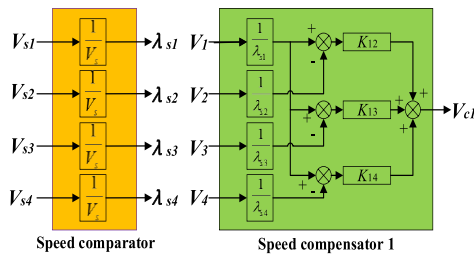

FIGURE 10. Speed comparator and compensator 1.

The improved relative coupling synchronous control scheme includes following two steps.

Step 1 (Speed Quantization):

Selecting ideal dive speed V_s as criterion, proportional quantification factor of tension winch i is calculated by

$$\lambda_{si} = V_{si}/V_s \quad (i = 1, 2, 3, 4) \quad (32)$$

where, V_{si} and λ_{si} denote the input speed and proportional quantification factor of tension winch i respectively.

Step 2 (Speed Compensation):

The proportional speed deviations between tension winch 1 and other tension winches are calculated by

$$\begin{cases} e_{12}(t) = V_1/\lambda_{s1} - V_2/\lambda_{s2} \\ e_{13}(t) = V_1/\lambda_{s1} - V_3/\lambda_{s3} \\ e_{14}(t) = V_1/\lambda_{s1} - V_4/\lambda_{s4} \end{cases} \quad (33)$$

where, $e_{1i}(t)(i = 2, 3, 4)$ denotes the proportional speed deviation between tension winch 1 and tension winch i.

The speed compensation value is obtained by

$$V_{c1} = K_{12}e_{12}(t) + K_{13}e_{13}(t) + K_{14}e_{14}(t) \quad (34)$$

where, $K_{1i}(i = 2, 3, 4)$ denotes the speed compensation factor between tension winch 1 and tension winch i.

Therefore, the actual input speed instruction of tension winch i can be given by

$$v_i = V_{si} - V_{ci}, \quad (i = 1, 2, 3, 4) \quad (35)$$

where, V_{si} denotes the input speed instruction of tension winch i generated by dive planning and general monitoring controller, V_{ci} denotes the speed compensation value.

Other speed compensators are designed in the same way. To avoid repetition, it is not described here.

D. CONTROLLER DESIGN OF LAYER 3
1) ALGORITHM ANALYSIS
Define state vector as $x := [\dot{\theta}_m T_s]^T$, the mathematical joint-space driven control model is transferred to following form according to (27).

$$\begin{cases} \dot{x}_1 = a_1 x_1 + a_2 x_2 + a_3 + \lambda_1 \\ \dot{x}_2 = b_1 x_1 + b_2 x_2 + b_3 u + \lambda_2 \\ y = x_1 \end{cases} \quad (36)$$

where, u denotes the control input, λ_1 and λ_2 are compound uncertainties with unknown upper bounds.

Since the joint-space hydraulic control model contains compound uncertainties with unknown upper bounds, to overcome model uncertainties and achieve adaptive robust control, an ARBFNN-BSMC algorithm is utilized for speed control of hydraulic winches. The scheme of ARBFNN-BSMC is shown in Fig. 11.
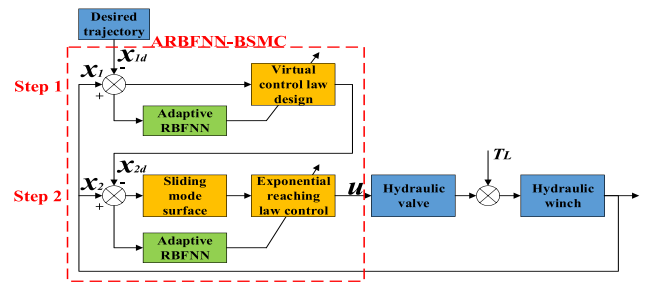

FIGURE 11. Structure of ARBFNN-BSMC algorithm.

The design philosophy of ARBFNN-BSMC algorithm is summarized as follows:

1) Backstepping design procedure is adopted to decompose the complex system into two subsystems. Lyapunov function and intermediate virtual control law are designed in each subsystem until the whole design procedure is finished. The asymptotic stability is ensured through backstepping design.

2) Sliding mode control method is employed at the second step to improve the system robustness, and exponential reaching law is utilized to enhance the convergence rate.

3) Adaptive RBF neural network is used for uncertainties estimation in intermediate virtual and actual control law design. Since RBF neural network is proved to have the ability of approximating any continuous function with arbitrary precision [29], the influences of

compound uncertainties with unknown upper bounds can be compensated, thus improving the anti-jamming ability and reducing the system chattering.

2) ARBFNN-BSMC DESIGN

The detailed backstepping design procedure of ARBFNN-BSMC is presented below.

Step 1: Design intermediate virtual control law x_{2d}, making speed tracking error z_1 converge to zero.

Define x_{1d} as the reference speed vector, assume $x_{1d}, \dot{x}_{1d}$, and $\ddot{x}_{1d}$ are all bounded variables.

Define error state variable as

$$\begin{cases} z_1 = x_1 - x_{1d} \\ z_2 = x_2 - x_{2d} \end{cases} \tag{37}$$

where, x_{2d} is the intermediate virtual control law.

The time derivative of first error state variable z_1 can be derived based on (36)-(37) as

$$\dot{z}_1 = a_1 x_1 + a_2 x_2 + a_3 + \lambda_1 - \dot{x}_{1d} \tag{38}$$

Treating x_2 as a control signal for (38), the virtual control law x_{2d} for x_2 which stabilizes z_1 is designed as

$$x_{2d} = \frac{1}{a_2}(-a_1 x_1 - a_3 + \dot{x}_{1d} - \lambda_1 - k_1 z_1) \tag{39}$$

Since λ_1 is unknown, a RBF neural network is used for uncertainty approximation, such that x_{2d} can be rewritten as

$$x_{2d} = \frac{1}{a_2}(-a_1 x_1 - a_3 + \dot{x}_{1d} - \lambda_{es1} - k_1 z_1) \tag{40}$$

where, λ_{es1} is designed using RBF neural network.

Define λ_{es1} as $\lambda_{es1} = \lambda_{e1} + \lambda_{s1}$, where λ_{e1} denotes the estimation of λ_1, and λ_{s1} denotes the designed term for estimate error compensation.

The function λ_{e1} is described utilizing RBF neural network as

$$\lambda_{e1} = W_1^T \phi(z_1, \xi_1) \tag{41}$$

where, W_1^T is the weight factor, $\phi(z_1, \xi_1)$ is radial gauss function, as presented below.

$$\phi(z_1, \xi_1) = \exp(-\frac{\|z_1 - \xi_1\|^2}{2b_\phi^2}) \tag{42}$$

where, ξ_1 is the center vector of hidden layer node, b_ϕ is the base width parameter, and $b_\phi > 0$.

Besides, the adaptive adjusting laws of W_1 and ξ_1 are designed as

$$\begin{aligned} \dot{W}_1 &= \mu_{11} \phi(z_1, \xi_1) z_1^T \\ \dot{\xi}_1 &= \mu_{12}(z_1^T W_1^T \phi_{\xi_1}'(z_1, \xi_1))^T \end{aligned} \tag{43}$$

where, μ_{11} and μ_{12} are adaptive adjusting factors.

Define estimate error as $\delta_1 = \lambda_1 - \lambda_{e1}$, to compensate for the estimate error, λ_{s1} is designed as

$$\lambda_{s1} = \frac{\hat{\delta}_1^2 z_1}{\hat{\delta}_1 |z_1| + \tau_1 e^{-at}} \tag{44}$$

where, $\hat{\delta}_1$ is the estimate value of δ_1, and the adaptive adjusting law of $\hat{\delta}_1$ is chosen as

$$\dot{\hat{\delta}}_1 = r_1 |z_1|, \, r_1 > 0 \tag{45}$$

Step 2: Sliding mode control with exponential reaching law is introduced to design the actual control law u, to make z_2 converge to a specified neighborhood around zero.

The time derivative of z_2 is obtained utilizing (36)-(37) and (40) as

$$\dot{z}_2 = b_1 x_1 + b_2 x_2 + b_3 u + \lambda_2 - \dot{x}_{2d} \tag{46}$$

An integral sliding mode surface is established with following structure

$$s = z_2 + \lambda_s \int z_2 dt \tag{47}$$

where, $\lambda_s > 0$ is the designed parameter.

The derivative of (47) is expressed by

$$\begin{aligned} \dot{s} &= \dot{z}_2 + \lambda_s z_2 \\ &= b_1 x_1 + b_2 x_2 + b_3 u + \lambda_2 - \dot{x}_{2d} + \lambda_s z_2 \end{aligned} \tag{48}$$

It has been proved in [30] and [31] that reaching law control has the ability to guarantee the convergence of closed-loop system trajectory onto the sliding manifold. Exponential reaching law is one of the widely used reaching laws, which is consisted of an exponential approaching item and a constant approaching item. Compared with constant rate reaching law, exponential reaching law has better approaching efficiency. Hence, following exponential reaching law is adopted.

$$\dot{s} = -k_2 s - \varepsilon \text{sgn}(s), \quad k_2 > 0, \, \varepsilon > 0 \tag{49}$$

The actual control law is designed as

$$u = u_{eq} + u_k + u_s \tag{50}$$

where, u_{eq} denotes the equivalent control item, u_k denotes the exponential approaching item, u_s represents the constant approaching item.

The equivalent control item is designed as

$$u_{eq} = -\frac{1}{b_3}[b_1 x_1 + b_2 x_2 - \dot{x}_{2d} + \lambda_s z_2 + \lambda_{e2}] \tag{51}$$

where, λ_{e2} is the estimation of λ_2, which is given by

$$\lambda_{e2} = W_2^T \phi(z_2, \xi_2) \tag{52}$$

The adjusting laws of W_2 and ξ_2 are designed as

$$\begin{aligned} \dot{W}_2 &= \mu_{21} \phi(z_2, \xi_2) s^T \\ \dot{\xi}_2 &= \mu_{22}(s^T W_2^T \phi_{\xi_2}'(z_2, \xi_2))^T \end{aligned} \tag{53}$$

where, μ_{21} and μ_{22} are adaptive adjusting factors.

The exponential approaching item is designed as

$$u_k = -\frac{k_2}{b_3}s \tag{54}$$

where, $k_2 > 0$.

The constant approaching item is designed as

$$u_s = -\frac{1}{b_3}[(\hat{\varphi}_2 + \eta_s)\text{sgn}(s)] \tag{55}$$

where, $\eta_s > 0$.

3) STABILITY ANALYSIS

The stability analysis of ARBFNN-BSMC can be illustrated by the proof of following two propositions.

Proposition 1: For the dynamic subsystem discussed in step 1, if z_2 converges to a specified neighborhood around zero, the tracking error $x_1 - x_{1d}$ is converged to zero asymptotically with the virtual control law x_{2d}.

Proof 1: It has been proved that the RBF neural network has the ability of approximating any continuous function with arbitrary precision. Therefore, λ_1 can be rewritten as

$$\lambda_1 = W_1^{*T}\phi(z_1, \xi_1^*) + \delta^*(z_1) \quad (56)$$

where, W_1^{*T} and ξ_1^* are the optimal weight and center of the Gaussian basis function respectively, $\delta^*(x)$ denotes the smallest approximate error.

Substituting (56) into (38) yields

$$\dot{z}_1 = a_1x_1 + a_2x_2 + a_3 + W_1^{*T}\phi(z_1, \xi_1^*) + \delta^*(z_1) - \dot{x}_{1d} \quad (57)$$

Based on (37) and (40), one can rewrite (57) as

$$\begin{aligned}
\dot{z}_1 &= a_1x_1 + a_2(z_2 + x_{2d}) + a_3 + W_1^{*T}\phi(z_1, \xi_1^*) \\
&\quad + \delta^*(z_1) - \dot{x}_{1d} \\
&= a_1x_1 + a_2z_2 + a_3 + W_1^{*T}\phi(z_1, \xi_1^*) + \delta^*(z_1) - \dot{x}_{1d} \\
&\quad - a_1x_1 - a_3 + \dot{x}_{1d} - \lambda_{e1} - \lambda_{s1} - k_1z_1 \\
&= a_2z_2 - k_1z_1 + W_1^{*T}\phi(z_1, \xi_1^*) + \delta^*(z_1) - \lambda_{e1} - \lambda_{s1}
\end{aligned} \quad (58)$$

The optimal radial gauss function $\phi(z_1, \xi_1^*)$ can be written in the form of Taylor's expansion as

$$\phi(z_1, \xi_1^*) = \phi(z_1, \xi_1) + \phi'_{\xi_1}\tilde{\xi}_1 + o(z_1, \tilde{\xi}_1) \quad (59)$$

where, ϕ'_{ξ_1} denotes partial derivative of $\phi(z_1, \xi_1^*)$ with respect to ξ_1, $\tilde{\xi}_1 = \xi_1^* - \xi_1$, $o(z_{s1}, \tilde{\xi}_1)$ denotes the higher order derivatives, and $|o(z_{s1}, \tilde{\xi}_1)| << |\phi(z_{s1}, \xi_1)| + |\phi'_{\xi_1}\tilde{\xi}_1|$.

Then the estimation error of λ_1 is calculated as

$$\begin{aligned}
\delta_1 &= \lambda_1 - \lambda_{e1} \\
&= W_1^{*T}\phi(z_1, \xi_1^*) + \delta(z_1) - W_1^T\phi(z_1, \xi_1) \\
&= W_1^{*T}(\phi(z_1, \xi_1) + \phi'_{\xi_1}\tilde{\xi}_1 + o(z_1, \tilde{\xi}_1)) \\
&\quad + \delta(z_1) - W_1^T\phi(z_1, \xi_1) \\
&= \tilde{W}_1^T\phi(z_1, \xi_1) + W_1^{*T}\phi'_{\xi_1}\tilde{\xi}_1 + W_1^{*T}o(z_1, \tilde{\xi}_1) + \delta(z_1) \\
&= \tilde{W}_1^T\phi(z_1, \xi_1) + W_1^T\phi'_{\xi_1}\tilde{\xi}_1 + \tilde{W}_1^T\phi'_{\xi_1}\tilde{\xi}_1 \\
&\quad + W_1^{*T}o(z_1, \tilde{\xi}_1) + \delta(z_1)
\end{aligned} \quad (60)$$

where, $\tilde{W}_1^T = W_1^{*T} - W_1^T$, define $\Gamma_1 = \tilde{W}_1^T\phi'_{\xi_1}\tilde{\xi}_1 + W_1^{*T}o(z_1, \tilde{\xi}_1) + \delta(z_1)$, and $|\Gamma_1| \le \delta_1$.

Substituting (60) into (58) yields

$$\dot{z}_1 = a_2z_2 - k_1z_1 + \tilde{W}_1^T\phi(z_1, \xi_1) + W_1^T\phi'_{\xi_1}\tilde{\xi}_1 + \Gamma_1 - \lambda_{s1} \quad (61)$$

Consider the first Lyapunov function candidate

$$\begin{aligned}
V_1 &= \tfrac{1}{2}z_1^2 + \tfrac{1}{2\mu_{11}}tr(\tilde{W}_1^T W_1) \\
&\quad + \tfrac{1}{2\mu_{12}}\tilde{\xi}_1^T\tilde{\xi}_1 + \tfrac{1}{2r_1}\tilde{\delta}_1^2 + \tfrac{\tau_1}{a}e^{-at}
\end{aligned} \quad (62)$$

where, $\tilde{\xi}_1 = \xi_1^* - \xi_1$, $\tilde{\delta}_1 = \hat{\delta}_1 - \delta_1$.

The derivative of (62) is obtained utilizing (43)-(45) as

$$\begin{aligned}
\dot{V}_1 &= z_1\dot{z}_1 - \frac{1}{\mu_{11}}tr(\tilde{W}_1^T\dot{W}_1) - \frac{1}{\mu_{12}}\tilde{\xi}_1^T\dot{\xi}_1 + \frac{1}{r_1}\tilde{\delta}_1\dot{\hat{\delta}}_1 - \tau_1 e^{-at} \\
&= z_1(a_2z_2 - k_1z_1 + \tilde{W}_1^T\phi(z_1, \xi_1) + W_1^T\phi'_{\xi_1}\tilde{\xi}_1 + \Gamma_1 - \lambda_{s1}) \\
&\quad - \frac{1}{\mu_{11}}tr(\tilde{W}_1^T\dot{W}_1) - \frac{1}{\mu_{12}}\tilde{\xi}_1^T\dot{\xi}_1 + (\hat{\delta}_1 - \delta_1)|z_1| - \tau_1 e^{-at} \\
&= z_1(a_2z_2 - k_1z_1 + \Gamma_1 - \lambda_{s1}) + (\hat{\delta}_1 - \delta_1)|z_1| - \tau_1 e^{-at}
\end{aligned} \quad (63)$$

Since

$$\begin{aligned}
& z_1(\Gamma_1 - \lambda_{s1}) + (\hat{\delta}_1 - \delta_1)|z_1| - \tau_1 e^{-at} \\
& \le \delta_1|z_1| - \frac{\hat{\delta}_1^2 z_1^2}{\hat{\delta}_1|z_1| + \tau_1 e^{-at}} + (\hat{\delta}_1 - \delta_1)|z_1| - \tau_1 e^{-at} \\
& = -\frac{\hat{\delta}_1^2 z_1^2}{\hat{\delta}_1|z_1| + \tau_1 e^{-at}} + \hat{\delta}_1|z_1| - \tau_1 e^{-at} \\
& = -\frac{\tau_1^2 e^{-2at}}{\hat{\delta}_1|z_1| + \tau_1 e^{-at}} \\
& \le 0
\end{aligned}$$

Following equation is obtained.

$$\begin{aligned}
\dot{V}_1 &\le a_2z_1z_2 - k_1z_1^2 \\
&\le \frac{|a_2|}{2\sigma}z_1^2 + \frac{\sigma|a_2|}{2}z_2^2 - k_1z_1^2 \\
&= -(k_1 - \frac{|a_2|}{2\sigma})z_1^2 + \frac{\sigma|a_2|}{2}z_2^2
\end{aligned} \quad (64)$$

where, $\sigma > 0$.

Obviously, it can be concluded form (64) that $\dot{V}_1 < 0$ as long as $z_1^2 > \frac{\sigma|a_2|}{2}z_2^2/(k_1 - \frac{|a_2|}{2\sigma})$. Consequently, the decrease of V_1 will eventually drives the tracking error $x_1 - x_{1d}$ into the boundary $|z_1| \le \sqrt{\frac{\sigma|a_2|}{2}z_2^2/(k_1 - \frac{|a_2|}{2\sigma})}$. Therefore, if z_2 converges to a specified neighborhood around zero, the tracking error z_1 is converged to zero. Hence, the dynamic subsystem 1 discussed in step 1 is conditionally asymptotically stable.

Proposition 2: For the dynamic subsystem discussed in step 2, the tracking error $x_2 - x_{2d}$ converges to zero asymptotically with the proposed control law u.

Proof 2: Substituting (50)-(51) and (54)-(55) into (48) yields

$$\begin{aligned}
\dot{s} &= b_1x_1 + b_2x_2 + b_3(u_{eq} + u_k + u_s) + \lambda_2 - \dot{x}_{2d} + \lambda_s z_2 \\
&= \lambda_2 - \lambda_{e2} - k_2s - (\hat{\varphi}_2 + \eta_s)\text{sgn}(s)
\end{aligned} \quad (65)$$

Following equation can be obtained utilizing the similar deriving method.

$$
\begin{aligned}
\delta_2 &= \lambda_2 - \lambda_{e2} \\
&= W_2^{*T}\phi(z_2, \xi_2^*) + \delta(z_2) - W_2^T\phi(z_2, \xi_2) \\
&= W_2^{*T}(\phi(z_2, \xi_2) + \phi'_{\xi_2}\tilde{\xi}_2 + o(z_2, \tilde{\xi}_2)) \\
&\quad + \delta(z_2) - W_2^T\phi(z_2, \xi_2) \\
&= \tilde{W}_2^T\phi(z_2, \xi_2) + W_2^T\phi'_{\xi_2}\tilde{\xi}_2 + \tilde{W}_2^T\phi'_{\xi_2}\tilde{\xi}_2 \\
&\quad + W_2^{*T}o(z_2, \tilde{\xi}_2) + \delta(z_2)
\end{aligned} \tag{66}
$$

where, $\tilde{W}_2^T = W_2^{*T} - W_2^T$, define also $\Gamma_2 = \tilde{W}_2^T\phi'_{\xi_2}\tilde{\xi}_2 + W_2^{*T}o(z_2, \tilde{\xi}_2) + \delta(z_2)$, and $|\Gamma_2| \leq \delta_2$.

Consider the second Lyapunov function candidate

$$
V_2 = \frac{1}{2}s^Ts + \frac{1}{2r_2}\tilde{\varphi}_2^2 + \frac{1}{2\mu_{21}}tr(\tilde{W}_2^TW_2) + \frac{1}{2\mu_{22}}\tilde{\xi}_2^T\tilde{\xi}_2 \tag{67}
$$

where, $\tilde{\xi}_2 = \xi_2^* - \xi_2$.

The derivative of (67) is calculated by

$$
\begin{aligned}
\dot{V}_2 &= s^T\dot{s} + \frac{1}{r_2}(\hat{\varphi}_2 - \varphi_2)\dot{\hat{\varphi}}_2 - \frac{1}{\mu_{21}}tr(\tilde{W}_2^T\dot{W}_2) - \frac{1}{\mu_{22}}\tilde{\xi}_2^T\dot{\xi}_2 \\
&= s^T\left[\lambda_2 - \lambda_{e2} - k_2s - (\hat{\varphi}_2 + \eta_s)\text{sgn}(s)\right] \\
&\quad + \frac{1}{r_2}(\hat{\varphi}_2 - \varphi_2)\dot{\hat{\varphi}}_2 - \frac{1}{\mu_{21}}tr(\tilde{W}_2^T\dot{W}_2) - \frac{1}{\mu_{22}}\tilde{\xi}_2^T\dot{\xi}_2
\end{aligned} \tag{68}
$$

The adaptive adjusting law of $\hat{\varphi}_2$ is designed as

$$
\dot{\hat{\varphi}}_2 = r_2|s| \tag{69}
$$

where, $r_2 > 0$.

Substituting (53), (66), and (69) into (68), one can obtain

$$
\begin{aligned}
\dot{V}_2 &= s^T\left[\lambda_2 - \lambda_{e2} - k_2s - (\hat{\varphi}_2 + \eta_s)\text{sgn}(s)\right] + (\hat{\varphi}_2 - \varphi_2)|s| \\
&\quad - tr(\tilde{W}_2^T\phi(z_2, \xi_2)s^T) - \tilde{\xi}_2^T(s^TW_2^T\phi'_{\xi_2}(z_2, \xi_2))^T \\
&= s^T\left[\Gamma_2 - (\hat{\varphi}_2 + \eta_s)\text{sgn}(s)\right] + (\hat{\varphi}_2 - \varphi_2)|s| \\
&\leq \varphi_2|s| - k_2s^2 - (\hat{\varphi}_2 + \eta_s)|s| + (\hat{\varphi}_2 - \varphi_2)|s| \\
&= -k_2s^2 - \eta_s|s| \\
&\leq 0
\end{aligned} \tag{70}
$$

Therefore, it is proved that with the sliding mode control law u, the system state can be guaranteed to stay on the sliding mode surface $s = 0$.

Moreover, solving (47) gives us

$$
z_2(t) = s(t) - \lambda_s e^{-\lambda_s t}\int_0^t s(\delta)e^{\lambda_s\delta}d\delta \tag{71}
$$

Based on (71), one can obtain

$$
\begin{aligned}
|z_2| &\leq |s| + \lambda_s e^{-\lambda_s t}\int_0^t |s|e^{\lambda_s\delta}d\delta \\
&= |s|(1 + \lambda_s e^{-\lambda_s t}\int_0^t e^{\lambda_s\delta}d\delta) \\
&= |s|(2 - e^{-\lambda_s t}) \\
&\leq 2|s|
\end{aligned} \tag{72}
$$

Hence, $s = 0$ can guarantee that the tracking error $x_2 - x_{2d}$ is converged to zero. Combined with the proof of proposition 1, the whole design procedure is proved to be stable.

IV. HARDWARE-IN-THE-LOOP SIMULATION
A. HARDWARE-IN-THE-LOOP SIMULATION SYSTEM
In this section, hardware-in-the-loop simulation [32] method is utilized. The scheme of hardware-in-the-loop simulation system we developed is shown in Fig. 12.
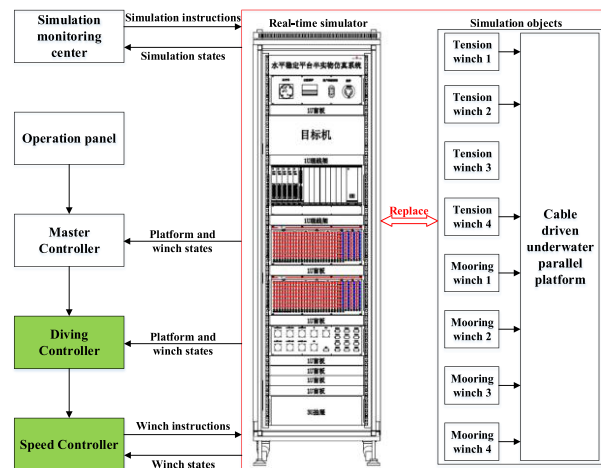

FIGURE 12. Scheme of hardware-in-the-loop simulation system.

The hardware-in-the-loop simulation system is mainly consisted of following six parts.

1) **Operation panel:** As human-computer interaction center, it provides the users with operating and monitoring interfaces.
2) **Master controller:** As the host of actual control system, it plays a role in mission assigning, integrated managing, and data analyzing.
3) **Diving controller:** It is responsible for dive planning and general monitoring, as well as synchronous controlling, which actually accomplish the tasks of layer 1 and layer 2.
4) **Speed controller:** It achieves closed-loop control of hydraulic winches.
5) **Real-time simulator:** It is used to simulate the real platform and driving mechanisms, and it is mainly consisted of real-time simulation engine, signal processing unit, and signal input/output interface. Once the simulation engine starts working, the information will be sent to actual controllers through signal input/output interface. Therefore, a complete closed loop is established to verify diving control strategies, algorithms, and interfaces.
6) **Simulation monitoring center:** It plays a role in developing, downloading, and debugging the program code, as well as monitoring simulation states.

B. VERIFICATION OF LAYER 3

Speed tracking control simulations are carried out under different kinds of unknown uncertainties, with PID control performance presented for comparison. The main parameters of underwater platform and hydraulic winches are shown in the Appendix. The simulation parameters are listed as follows.

1) Ideal speed trajectories: sinusoidal curve, ramp curve, and diving curve.
2) Regularly changed compound uncertainties: $\lambda_1 = 0.02\cos(x_1 * x_1)$, $\lambda_2 = 20\cos(x_2 * x_2)$.
3) Regularly and suddenly changed compound uncertainties:

$$\lambda_1 = \begin{cases} 0.02\cos(x_1 * x_1), & t \neq 12s \\ 20\cos(x_1 * x_1), & t = 12s; \end{cases}$$

$$\lambda_2 = \begin{cases} 20\cos(x_2 * x_2), & t \neq 12s \\ 20000\cos(x_2 * x_2), & t = 12s. \end{cases}$$

4) Controller parameters: $k_1 = 15$, $k_2 = 1.5$, $\lambda_s = 16.1$, $\eta_s = 0.01$, $r_1 = 0.2$, $r_2 = 0.1$, $\tau_1 = 1$, $a = 0.01$, the adopted RBF neural network contains three nodes in the hidden layer, and the network learning parameters are selected as $\mu_{11} = \mu_{12} = 0.05$, $\mu_{21} = \mu_{22} = 0.1$.

The speed control trajectories under regularly changed compound uncertainties are presented in Fig. 13, and the data analyses are summarized in Table 1. We observed that both PID controller and proposed controller can achieve speed tracking under regularly changed compound uncertainties. However, compared with PID controller, proposed controller shows better stability in adjusting period and higher steady-state precision. Besides, barely any overshoot occurs to the proposed control performance. In general, the proposed controller performs better than PID controller in speed control simulation under regularly changed compound uncertainties.
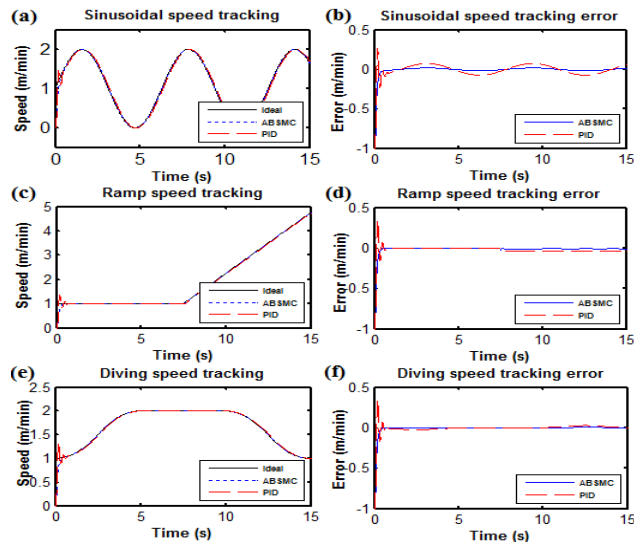
TABLE 1. Data analyses of speed control simulation under regularly changed compound uncertainties.

Ideal speed	Parameter	ABSMC	PID
Sinusoidal curve	Average value of absolute steady-state error (m/min)	0.0097	0.0451
	Maximum value of absolute steady-state error (m/min)	0.0168	0.0733
	Maximum overshoot during adjusting period (m/min)	0.0001	0.2214
Ramp curve	Average value of absolute steady-state error (m/min)	0.0046	0.0202
	Maximum value of absolute steady-state error (m/min)	0.0242	0.0479
	Maximum overshoot during adjusting period (m/min)	0.0002	0.3439
Diving curve	Average value of absolute steady-state error(m/min)	0.0022	0.0099
	Maximum value of absolute steady-state error (m/min)	0.0068	0.0293
	Maximum overshoot during adjusting period (m/min)	0.0001	0.3409

To further verify the capability of disturbance resisting, amplitudes of compound disturbances are suddenly increased at 12 s. The speed control trajectories under regularly and suddenly changed compound uncertainties are presented in Fig. 14, and the data analyses are summarized in Table 2. When system compound uncertainties suddenly increase, fluctuations are observed in the speed tracking control performances of both PID controller and proposed controller. However, it takes longer adjusting time and more oscillations for PID controller to make the trajectories back to normal. Besides, as shown in Table 2, the maximum absolute speed tracking errors of PID controller caused by suddenly changed compound uncertainties are bigger than proposed controller. Therefore, it can be concluded that the proposed controller has better capability of disturbance resisting when dealing with suddenly changed uncertainties.
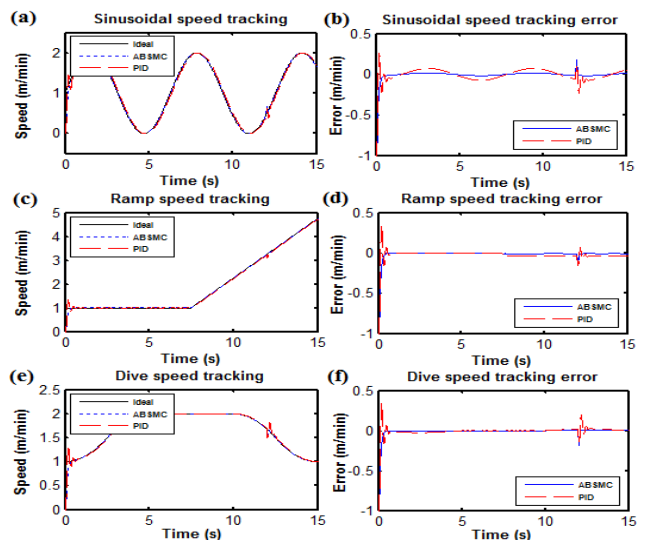

FIGURE 13. Speed control simulation under regularly changed compound uncertainties.

FIGURE 14. Speed control simulation under regularly and suddenly changed compound uncertainties.

TABLE 2. Data analyses of adjusting period when dealing with suddenly changed compound uncertainties.

Ideal speed	Parameter	ABSMC	PID
Sinusoidal curve	Maximum absolute error (m/min)	0.1828	0.2324
	Adjustment period (s)	0.13	0.45
	Oscillation times	1	3
Ramp curve	Maximum absolute error (m/min)	0.1013	0.1598
	Adjustment period (s)	0.12	0.42
	Oscillation times	1	3
Diving curve	Maximum absolute error (m/min)	0.1425	0.1911
	Adjustment period (s)	0.15	0.62
	Oscillation times	1	4

Taken together the speed tracking control performance of the two controllers under different tasks and working conditions, the proposed controller shows higher precision, better stability, and better capability of disturbance resisting, thus is more suitable for speed control of hydraulic winches.

C. VERIFICATION OF LAYER 2

Although ARBFNN-BSMC has been proved to have good anti-jamming capability, fluctuations still occur when compound uncertainties suddenly increase. If different uncertainties occur to the winches with different amplitudes, speed control synchronization between each driving branch will be affected. To verify the feasibility of proposed synchronous control scheme, speed tracking control simulation of four tension winches are carried out in two different conditions.

In the first condition, transient different uncertainties occur to four tension winches at 10 s, and the compound uncertainties are designed as follows: 1) Winch 1: $\lambda_1 = 10 \cos(x_1 * x_1)$; 2) Winch 2: $\lambda_1 = 30 \cos(x_1 * x_1)$; 3) winch 3: $\lambda_1 = 50 \cos(x_1 * x_1)$; 4) winch 4: $\lambda_1 = 70 \cos(x_1 * x_1)$. In the second condition, long-term different uncertainties occur to four tension winches after 7.5 s, and the compound uncertainties are designed as: 1) Winch 1: $\lambda_1 = 0.02 \cos(x_1 * x_1) - 2$; 2) Winch 2: $\lambda_1 = 0.02 \cos(x_1 * x_1) - 4$; 3) winch 3: $\lambda_1 = 0.02 \cos(x_1 * x_1) - 6$; 4) winch 4: $\lambda_1 = 0.02 \cos(x_1 * x_1) - 8$.

Simulation results are shown in Fig. 15 and Fig. 16 respectively. Fig. 15 (a) and Fig. 16 (a) show the speed tracking trajectories of four tension winches without synchronous control, whereas Fig. 15 (b) and Fig. 16 (b) shows the speed tracking performances with synchronous control. The speed tracking performances of four tension winches show distinct differences when different compound uncertainties occur. However, once synchronous control strategy works, speed tracking deviations between each winch decrease significantly, which proves that the synchronous control strategy is effective.

Moreover, the data analyses of Fig. 16 are summarized in Table 3 and Table 4.

The data also show that compared with speed tracking without synchronous control, the average speed derivations between four winches are significantly reduced when proposed synchronous control strategy starts to work.
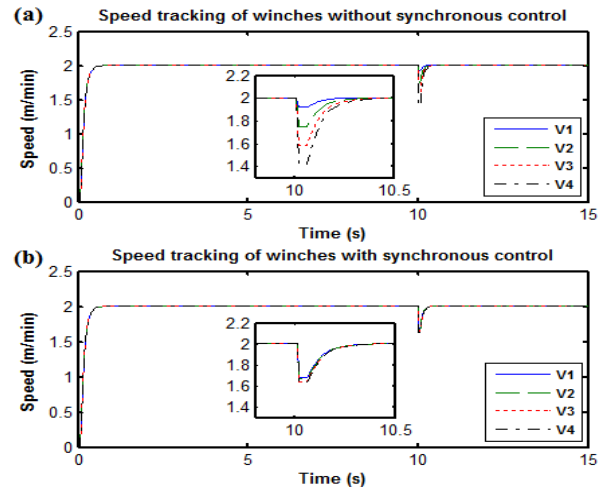

FIGURE 15. Speed tracking control of four tension winches under transient different uncertainties.
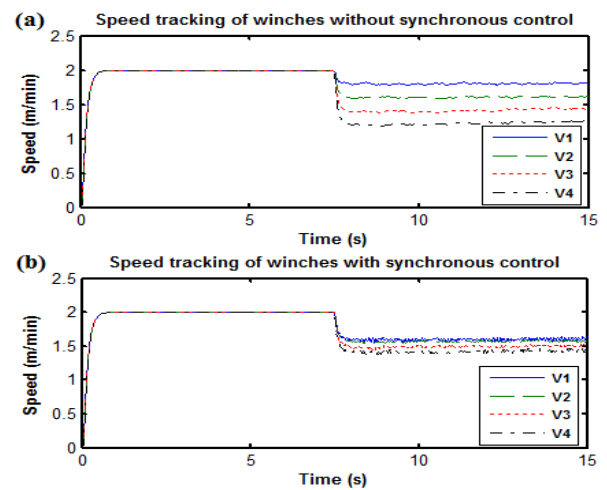

FIGURE 16. Speed tracking control of four tension winches under long-term different uncertainties.

TABLE 3. Average performance in Fig. 16 (a) after 7.5 s.

Parameter	Value	Parameter	Value
V_1	1.805	V_2	1.611
e_{12}	0.194	e_{21}	-0.194
e_{13}	0.385	e_{23}	0.191
e_{14}	0.573	e_{24}	0.379
V_3	1.420	V_4	1.232
e_{31}	-0.385	e_{41}	-0.573
e_{32}	-0.191	e_{42}	-0.379
e_{34}	0.188	e_{43}	-0.188

Based on the above analyses, it is proved that whether transient or long-term different uncertainties occur, the improved relative coupling synchronous control strategy is effective to enhance the speed control synchronization.

D. VERIFICATION OF LAYER 1

To verify the speed adjusting function of layer 1, diving control simulations are carried out in four different unsatisfactory conditions. The ideal speed instructions are selected

TABLE 4. Average performance in Fig. 16 (b) after 7.5 s.

Parameter	Value	Parameter	Value
V_1	1.604	V_2	1.575
e_{12}	0.029	e_{21}	-0.029
e_{13}	0.103	e_{23}	0.074
e_{14}	0.177	e_{24}	0.148
V_3	1.501	V_4	1.427
e_{31}	-0.103	e_{41}	-0.177
e_{32}	-0.074	e_{42}	-0.148
e_{34}	0.074	e_{43}	-0.074

as $V_{t1} = V_{t2} = V_{t3} = V_{t4} = 2 \text{m/min}$, and the speed adjusting factors are $\varepsilon_1 = \varepsilon_2 = \varepsilon_3 = \varepsilon_4 = 80$. The initial attitudes of platform in the four different unsatisfactory conditions are selected as: 1) $\alpha = 3°$, $\beta = 2°$; 2) $\alpha = 3°$, $\beta = -2°$; 3) $\alpha = -3°$, $\beta = 2°$; 4) $\alpha = -3°$, $\beta = -2°$.

The diving control simulation results in four working conditions are shown in Fig. 17-Fig. 20.

FIGURE 17. Diving control simulation with initial attitude $\alpha = 3°$, $\beta = 2°$.

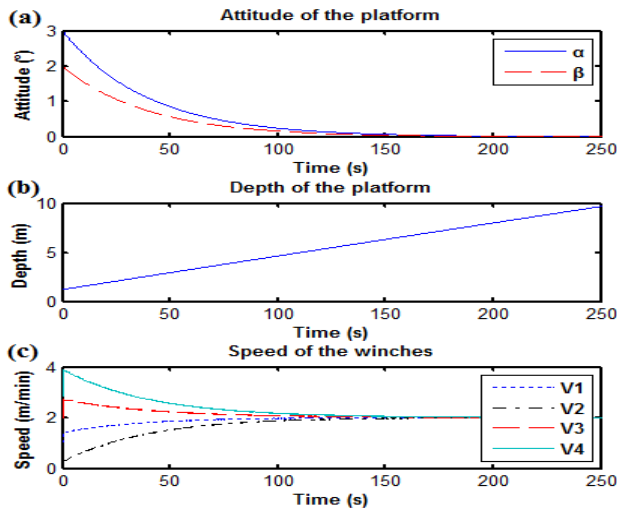**FIGURE 18.** Diving control simulation with initial attitude $\alpha = 3°$, $\beta = -2°$.
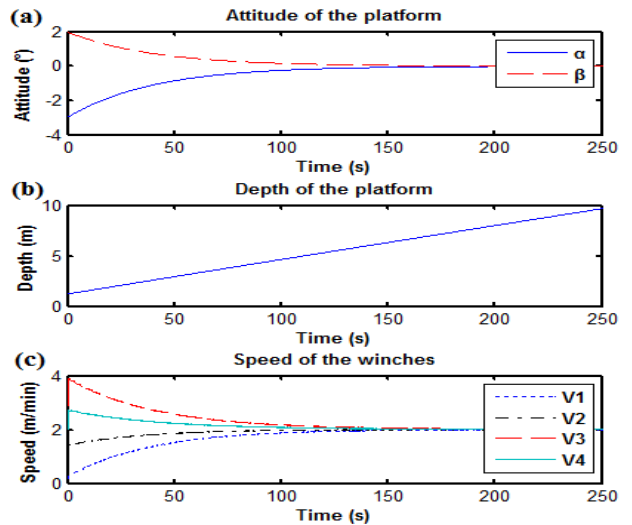
FIGURE 19. Diving control simulation with initial attitude $\alpha = -3°$, $\beta = 2°$.

The simulation results show that the dive planning and general monitoring controller we developed for layer 1 can adjust the attitudes of platform smoothly to ideal state under four different unsatisfactory working conditions without oscillation, which can lay good foundation for steady diving control regardless of the unsatisfactory working conditions. Hence, the effectiveness of layer 1 is proved.

Moreover, to verify the function of speed adjusting factors, diving control simulations are carried out under different speed adjusting factors. The simulation results are shown in Fig. 21.

Following conclusions can be drawn from the above-mentioned simulation results:

1) Under the function of diving strategy planning and online monitoring, steady diving process can be achieved despite unsatisfactory working conditions.
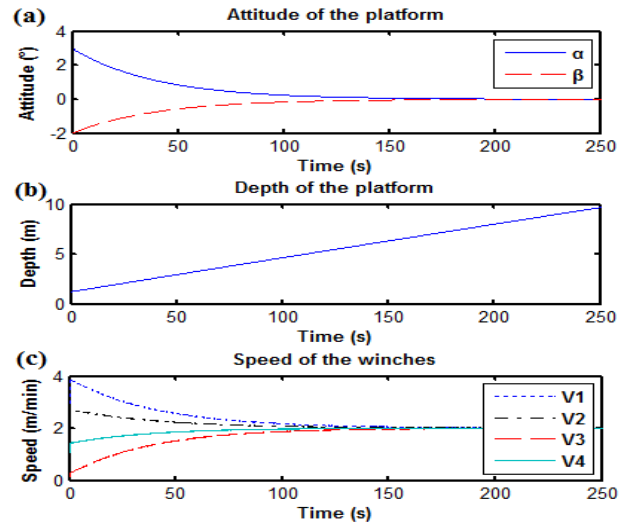
2) As speed adjusting factor increases, the attitude adjusting period becomes longer, and the attitude adjusting efficiency is lower.

Based on the hardware-in-the-loop simulation results of layer 1, layer 2, and layer 3, feasibility of our approach is verified. Hence, the proposed three-layer adaptive diving control strategy is proved to be suitable for the diving control of underwater cable-driven parallel platform.

V. EXPERIMENT
A. EXPERIMENT PREPARATION
To further verify the efficiency of proposed approach, early-stage experiments are implemented in a lake. The lake depth is about 150 m, and the average velocity of the current is about 0.5 knots.

The implementing process include following steps:

1) **Towing:** The platform is towed to the experiment area by a mother ship;

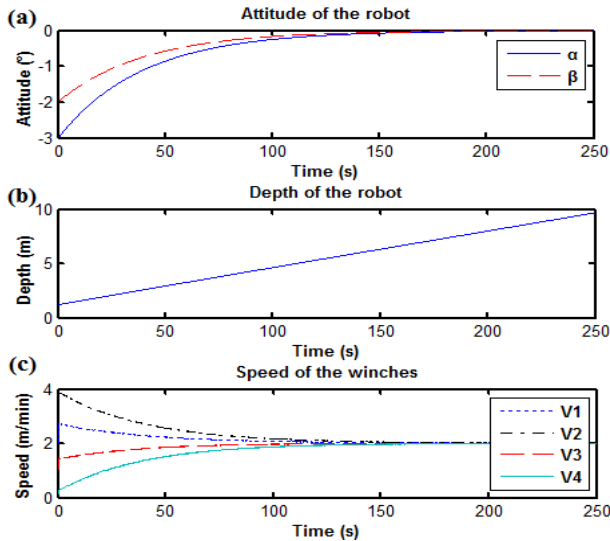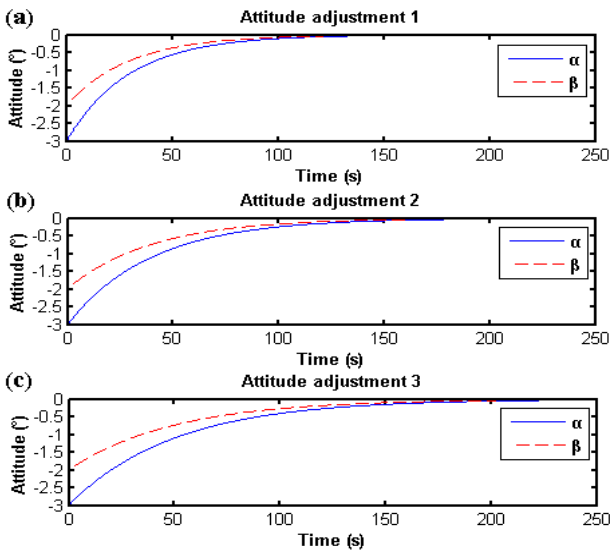**FIGURE 20.** Diving control simulation with initial attitude $\alpha = -3°$, $\beta = -2°$.

FIGURE 21. Attitude adjustment with different speed adjusting factors. (a) $\varepsilon = 60$; (b) $\varepsilon = 80$; (c) $\varepsilon = 100$.

2) **Ballast adjusting:** The ballast of platform are adjusted by culvert system;
3) **Anchoring:** Four gravity anchors are put to the bottom of the lake by hydraulic winches;
4) **Diving:** The platform dives to the specific depth according to the requirements;
5) **Experiment:** Scientific experiment is implemented on the platform;
6) **Recycling:** The platform is recycled and towed back to the shore side.

The main driving and measuring facilities used for the experiment are summarized in Table 5.

Besides, it has to be noted that the inclinometer is installed at the center of platform surface, and the four depth meters

TABLE 5. Main driving and measuring facilities.

Facility	Type	Main characteristics
Hydraulic motor	MRH750	Rated speed: 400 rpm; Rated flow: 70L/min.
Cable	Galvanized steel core wire	ZAA6×36WS; Strength of extension: 1870MPa
Depth meter	miniIPS	Range: 0-100 m; Precision: ±0.01 m
Inclinometer	SST300	Range: ±10°; Precision: ±0.01°

are installed near the points A_i, $i = 1, 2, 3, 4$, which are the action spots of four tension cables.

B. EXPERIMENT RESULTS

The results of two experiments are demonstrated below.

In the first experiment, the desired diving velocity of platform is selected as 1.5 m/min. The diving performances of the platform between 10 m and 40 m are demonstrated in Fig. 22, and the data analyses are summarized in Table 6.

FIGURE 22. Diving performances of the platform between 10 m and 40 m in the first experiment.

TABLE 6. Data analyses of the first experiment.

Parameter	Average	Maximum	Minimum
Absolute depth error (m)	0.268	0.437	0.001
Absolute velocity error (m/min)	0.025	0.042	0.011
Percentage of absolute velocity error	1.67%	2.80%	0.73%
Absolute angle of heeling (°)	0.569	0.642	0.472
Absolute angle of trimming (°)	0.314	0.352	0.277

In the second experiment, the desired diving velocity of platform is selected as 2.0 m/min. The diving performances of the platform between 20 m and 50 m are demonstrated in Fig. 23, and the data analyses are summarized in Table 7.
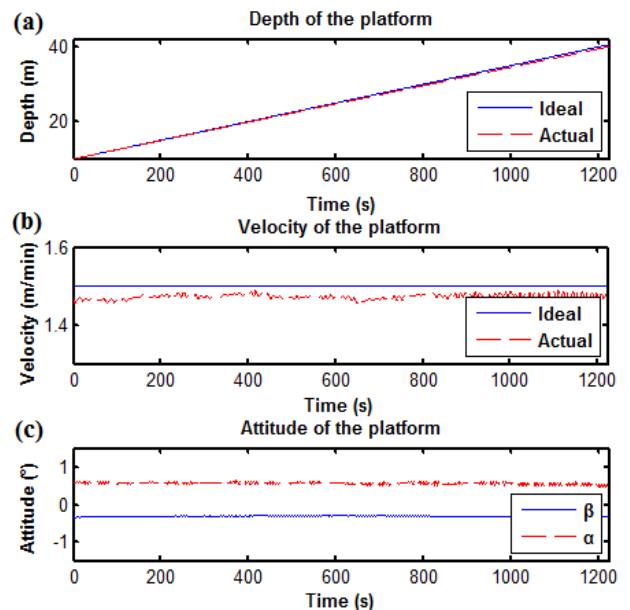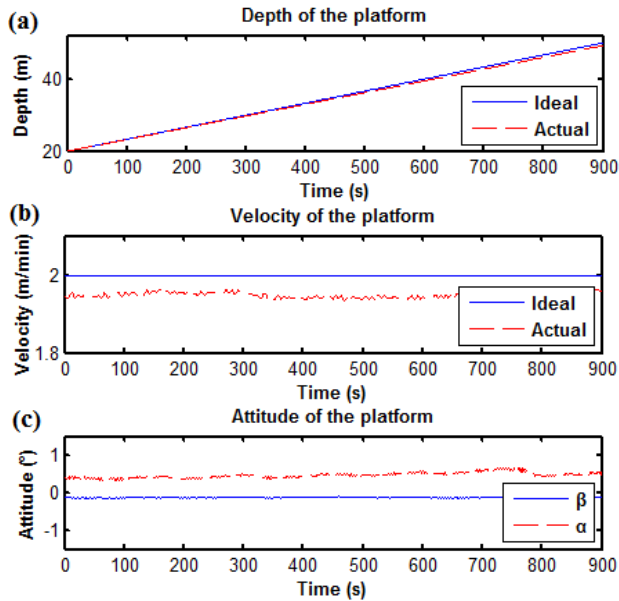

FIGURE 23. Diving performances of the platform between 20 m and 50 m in the second experiment.

TABLE 7. Data analyses of the second experiment.

Parameter	Average	Maximum	Minimum
Absolute depth error (m)	0.327	0.479	0.001
Absolute velocity error (m/min)	0.051	0.066	0.030
Percentage of absolute velocity error	2.55%	3.30%	1.5%
Absolute angle of heeling (°)	0.476	0.683	0.308
Absolute angle of trimming (°)	0.119	0.151	0.091

Fig. 22 (a) and Fig. 23 (a) clearly indicate that the underwater cable-driven platform can dive along the desired depth trajectories closely utilizing the proposed approach. Moreover, according to the calculating data in Table 4 and Table 5, the average percentages of absolute velocity error during diving process are 1.67% and 2.55%, which are both smaller than the required 5%. Besides, attitudes of platform during the two diving process are much better than the requirements. Therefore, it is verified through lake experiments that the proposed approach can achieve high precision diving control with required velocity and attitude. However, oscillations are observed in velocity and attitude trajectories, the elimination of which will need future research.

VI. CONCLUSIONS

To achieve high precision diving control of a new cable-driven underwater parallel platform for a special scientific application, modeling, controller design, and experiment are studied in the current work. The platform is analyzed within a three degrees-of-freedom framework utilizing a simplified modeling approach, and the driven control model is established based on joint-space method. Subsequently, a three-layer adaptive diving control strategy is proposed, which is mainly consisted of dive planning and general monitoring layer, synchronous control layer, and speed control layer. Improved relative coupling control strategy is utilized to enhance the synchronization between multiple hydraulic winches. Robustness to system uncertainties is addressed by adopting an adaptive RBFNN based backstepping sliding mode control method for single drive branch control.

At present, the design and implementation of diving control system for cable-driven underwater parallel platform

TABLE 8. Main parameters of cable-driven underwater parallel platform

Symbol	Parameter	Value
a_0	Length	50.4 m
b_0	width	18 m
c_0	Height	2 m
$a'/2$	Longitudinal actuating arm length of tension cable	23.7 m
$b'/2$	Lateral actuating arm length of tension cable	7.5 m
$a''/2$	Longitudinal actuating arm length of mooring cable	25.2 m
$b''/2$	Lateral actuating arm length of mooring cable	7.5 m
m_1	Mass	2328.86 t
Δm	Additional mass	1.32×10^7 kg
I_x	Lateral inertia tensor	4.93×10^8 kg.m^2
I_y	Longitudinal inertia tensor	6.29×10^7 kg.m^2
ΔI_x	Additional lateral inertia tensor	2.05×10^8 kg.m^2
ΔI_y	Additional longitudinal inertia tensor	2.0×10^9 kg.m^2

TABLE 9. Main parameters of hydraulic drive system.

Symbol	Parameter	Value
r	Roll radius	0.768 m
n	Reduction ratio	536
K	Gain of proportional valve	1.25×10^{-3} m/V
C_d	Flow coefficient of valve port	0.61
ω	Valve area gradient	0.785 m
P_s	Oil-supply pressure of pump	1.5×10^7 Pa
ρ	Hydraulic oil density	850 kg/m^3
D_m	Theoretical volumetric displacement of hydraulic motor	150 ml/r
V_m	Total volume of actuation mechanism	1.47×10^{-3} m^3
β_e	Bulk modulus	7.0×10^8 Pa
C_{tm}	The total leakage coefficient	1.9×10^{-11} m^5/(N•s)
J_m	Total inertia	152.06 kg•m^2
B_m	Viscous damping coefficient	800 N•s/m
P_L	External load pressure	1.1×10^7 Pa

has been completed, and the feasibility has been validated by hardware-in-the-loop simulations and early-stage lake experiments. However, considering the more unpredictable and harsh experimental environment in the ocean, more field trials should be carried out, and better disturbance prediction mechanism and control parameters optimization strategy should be concerned. This warrants further research.

APPENDIX
See Tables 8 and 9.

REFERENCES

[1] X. Xiang, C. Yu, and Q. Zhang, "On intelligent risk analysis and critical decision of underwater robotic vehicle," *Ocean Eng.*, vol. 140, pp. 453–465, Aug. 2017.

[2] G. Nawratil, "Stewart Gough platforms with non-cubic singularity surface," *Mech. Mach. Theory*, vol. 45, no. 12, pp. 1851–1863, Dec. 2010.

[3] B. Rohani, Y. Yazicioglu, M. Mutlu, O. Ogucu, E. Akgul, and A. Saranli, "Lagrangian based mathematical modeling and experimental validation of a planar stabilized platform for mobile systems," *J. Comput. Appl. Math.*, vol. 259, no. 2, pp. 955–964, Mar. 2014.

[4] B. K. Sarkar, "Modeling and validation of a 2-DOF parallel manipulator for pose control application," *Robot. Comput.-Integr. Manuf.*, vol. 50, pp. 234–241, Apr. 2018.

[5] C. T. Orlowski and A. R. Girard, "Dynamics, stability, and control analyses of flapping wing micro-air vehicles," *Prog. Aerosp. Sci.*, vol. 51, pp. 18–30, May 2012.

[6] J. Guo, H. He, and C. Sun, "Analysis of the performance of aerial work platform working device based on virtual prototype and finite element method," *Energy Procedia*, vol. 104, pp. 568–573, Dec. 2016.

[7] P. Long, W. Khalil, and P. Martinet, "Dynamic modeling of parallel robots with flexible platforms," *Mech. Mach. Theory*, vol. 81, pp. 21–35, Nov. 2014.

[8] J. Wu, G. Yu, Y. Gao, and L. Wang, "Mechatronics modeling and vibration analysis of a 2-DOF parallel manipulator in a 5-DOF hybrid machine tool," *Mech. Mach. Theory*, vol. 121, pp. 430–445, Mar. 2018.

[9] A. V. Nguyen, B. C. Bouzgarrou, K. Charlet, and A. Béakou, "Static and dynamic characterization of the 6-Dofs parallel robot 3CRS," *Mech. Mach. Theory*, vol. 93, pp. 65–82, Nov. 2015.

[10] M. M. Horoub, M. Hassan, and M. A. Hawwa, "Workspace analysis of a Gough-Stewart type cable marine platform subjected to harmonic water waves," *Mech. Mach. Theory*, vol. 120, pp. 314–325, Feb. 2018.

[11] K. Cai *et al.*, "Modeling and controller design of a 6-DOF precision positioning system," *Mech. Syst. Signal Process.*, vol. 104, pp. 536–555, May 2018.

[12] S. Mahapatra, B. Subudhi, R. Rout, and B. V. S. S. K. Kumar, "Nonlinear H_∞ Control for an autonomous underwater vehicle in the vertical plane," *IFAC-PapersOnLine*, vol. 49, no. 1, pp. 391–395, Feb. 2016.

[13] C. Edwards and Y. B. Shtessel, "Adaptive continuous higher order sliding mode control," *Automatica*, vol. 65, pp. 183–190, Mar. 2016.

[14] X. Xiang, C. Liu, H. Su, and Q. Zhang, "On decentralized adaptive full-order sliding mode control of multiple UAVs," *ISA Trans.*, vol. 71, pp. 196–205, Nov. 2017.

[15] H. Li, J. Yu, C. Hilton, and H. Liu, "Adaptive sliding-mode control for nonlinear active suspension vehicle systems using T–S fuzzy approach," *IEEE Trans. Ind. Electron.*, vol. 60, no. 8, pp. 3328–3338, Aug. 2013.

[16] S.-H. Chen and L.-C. Fu, "Observer-based backstepping control of a 6-dof parallel hydraulic manipulator," *Control Eng. Pract.*, vol. 36, pp. 100–112, Mar. 2015.

[17] M. A. Toso and H. M. Gomes, "A smart force platform using artificial neural networks," *Measurement*, vol. 91, pp. 124–133, Sep. 2016.

[18] K. Shojaei, "Neural network formation control of underactuated autonomous underwater vehicles with saturating actuators," *Neurocomputing*, vol. 194, pp. 372–384, Jun. 2016.

[19] D. Ginoya, P. D. Shendge, and S. B. Phadke, "Disturbance observer based sliding mode control of nonlinear mismatched uncertain systems," *Commun. Nonlinear Sci. Numer. Simul.*, vol. 26, nos. 1–3, pp. 98–107, Sep. 2015.

[20] M. A. Mirza, S. Li, and L. Jin, "Simultaneous learning and control of parallel Stewart platforms with unknown parameters," *Neurocomputing*, vol. 266, pp. 114–122, Nov. 2017.

[21] J. Fang, R. Yin, and X. Lei, "An adaptive decoupling control for three-axis gyro stabilized platform based on neural networks," *Mechatronics*, vol. 27, pp. 38–46, Apr. 2015.

[22] B.-L. Zhang, A.-M. Feng, and J. Li, "Observer-based optimal fault-tolerant control for offshore platforms," *Comput. Elect. Eng.*, vol. 40, no. 7, pp. 2204–2215, Oct. 2014.

[23] L. Lapierre and B. Jouvencel, "Robust nonlinear path-following control of an AUV," *IEEE J. Ocean. Eng.*, vol. 33, no. 2, pp. 89–102, Apr. 2008.

[24] H. Nourisola, B. Ahmadi, and S. Tavakoli, "Delayed adaptive output feedback sliding mode control for offshore platforms subject to nonlinear wave-induced force," *Ocean Eng.*, vol. 104, pp. 1–9, Aug. 2015.

[25] Y. Xia, G. Xu, K. Xu, Y. Chen, X. Xiang, and Z. Ji, "Dynamics and control of underwater tension leg platform for diving and leveling," *Ocean Eng.*, vol. 109, pp. 454–478, Nov. 2015.

[26] B.-L. Zhang, Q.-L. Han, X.-M. Zhang, and X. Yu, "Integral sliding mode control for offshore steel jacket platforms," *J. Sound Vibrat.*, vol. 331, no. 14, pp. 3271–3285, Jul. 2012.

[27] T. I. Fossen, *Guidance and Control of Ocean Vehicles*. New York, NY, USA: Wiley, 1994, pp. 6–55.

[28] Z. S. Wu, *Hydraulic Control Systems*. Beijing, China: Chinese Higher Education Press, 2008, pp. 56–58.

[29] J. Park and I. W. Sandberg, "Universal approximation using radial-basis-function networks," *Neural Comput.*, vol. 3, no. 2, pp. 246–257, Jan. 1991.

[30] X. Huang, C. Zhang, H. Lu, and M. Li, "Adaptive reaching law based sliding mode control for electromagnetic formation flight with input saturation," *J. Franklin Inst.*, vol. 353, no. 11, pp. 2398–2417, Jul. 2016.

[31] H. Wang, X. Zhao, and Y. Tian, "Trajectory tracking control of XY table using sliding mode adaptive control based on fast double power reaching law," *Asian J. Control*, vol. 18, no. 6, pp. 2263–2271, Nov. 2016.

[32] P. Sarhadi, A. R. Noei, and A. Khosravi, "Model reference adaptive autopilot with anti-windup compensator for an autonomous underwater vehicle: Design and hardware in the loop implementation results," *Appl. Ocean Res.*, vol. 62, pp. 27–36, Jan. 2017.

YINGKAI XIA was born in Henan, China, in 1989. He received the B.S. and Ph.D. degrees in naval architecture and ocean engineering from the Huazhong University of Science and Technology, Wuhan, China, in 2011 and 2017, respectively.

He currently holds a post-doctoral position at the School of Naval Architecture, Ocean and Civil Engineering, Shanghai Jiao Tong University. His current research interests include design of underwater equipment, dynamic modeling and adaptive control of complex nonlinear systems, renewable energy technology, and ocean engineering.

KAN XU was born in Hubei, China, in 1990. She received the B.S. degree in control science and engineering and the M.S. degree in naval architecture and ocean engineering from the Huazhong University of Science and Technology, Wuhan, China, in 2011 and 2014, respectively.

She is currently an Engineer with the Wuhan Second Ship Design and Research Institute. Her current research interests include design of submarine, intelligent control of complex nonlinear systems, and system development.

YE LI (M'98–SM'10) was born in Beijing, China, in 1977. He received the B.S. degree in naval architecture and ocean engineering from Shanghai Jiao Tong University, Shanghai, China, in 2000, and the M.S. and Ph.D. degrees in mechanical engineering from The University of British Columbia, Canada, in 2004 and 2007, respectively.

From 2007 to 2009, he was a Research Assistant with the Advanced Power and Energy System Group, Energy Technology Division, Pacific Northwest National Laboratory, USA. From 2009 to 2013, he was Senior Research Scientist and the Founding Lead of the Offshore Energy Modeling Group, National Wind Technology Center, National Renewable Energy Laboratory, USA. He is currently a Professor with the School of Naval Architecture, Ocean and Civil Engineering, Shanghai Jiao Tong University, the Director of Shanghai Jiao Tong University Multiple functional towing tank, and the Director of the NRDC National Center for Offshore Wind Technology. His current research interests include marine hydrodynamics, renewable energy technology, and mathematical modeling of complex system behavior.

XIANBO XIANG (S'09–M'12) was born in Hubei, China in 1978. He received the B.S. and M.S. degrees in automatic control and marine engineering from the Huazhong University of Science and Technology, China, in 2000 and 2003, respectively, and the Ph.D. degree in robotics from the University of Montpellier 2, Montpellier, France, in 2011.

From 2006 to 2006, he was an EC Erasmus Mundus Visiting Scholar with the SpaceMaster Project. From 2008 to 2011, he was involved in the European Project FreeSubNet as an EC Marie Curie ESR Fellow at LIRMM, CNRS UMR 5506, France. He is currently an Associate Professor with the School of Naval Architecture and Ocean Engineering, Huazhong University of Science and Technology. His research interests include nonlinear control of nonholonomic mobile robot and underactuated autonomous underwater vehicle, and coordinated control of multiple autonomous vehicles.

• • •

GUOHUA XU was born in Hubei, China, in 1964. He received the B.S. and M.S. degrees in automation from the Wuhan University of Technology, Wuhan, China, in 1986 and 1991 respectively, and the Ph.D. degree in mechatronic engineering from the Huazhong University of Science and Technology, Wuhan, China, in 2005.

From 1986 to 1991, he was a Research Assistant with the Wuhan University of Technology, Wuhan, China. He is currently a Professor with the School of Naval Architecture and Ocean Engineering, Huazhong University of Science and Technology, the Director of the Marine Engineering Department, the Deputy Director of the Hubei Ships and Marine Hydrodynamics Key Laboratory, and the Director of the Institute of Intelligent Machinery and Control. His research interests include complex marine system development, underwater operation, intelligent control of underwater vehicle, and ocean engineering.